

This manuscript has been submitted to the ISPRS Journal of Photogrammetry and Remote Sensing. Please note that this manuscript is currently under peer review and has not been formally accepted for publication. Subsequent versions of this manuscript may have slightly different content.

Deep learning with simulated laser scanning data for 3D point cloud classification

Alberto M. Esmorís^{a,e}, Hannah Weiser^a, Lukas Winiwarter^{a,c,d}, Jose C. Cabaleiro^{e,f}, Bernhard Höfle^{a,b,*}

^a*3DGeo Research Group, Institute of Geography, Heidelberg University, Im Neuenheimer Feld
368, Heidelberg, 69120, Baden-Württemberg, Germany*

^b*Interdisciplinary Center for Scientific Computing (IWR), Heidelberg University, Im Neuenheimer Feld
205, Heidelberg, 69120, Baden-Württemberg, Germany*

^c*Research Unit Photogrammetry, Department of Geodesy and Geoinformation, TU Wien, Wiedner Hauptstraße
8-10, Vienna, 1040, Vienna, Austria*

^d*Integrated Remote Sensing Studio, Faculty of Forestry, The University of British Columbia, 2424 Main Mall, Vancouver, V6T 1Z4, British
Columbia, Canada*

^e*Centro Singular de Investigación en Tecnoloxías Intelixentes, Universidade de Santiago de Compostela, Rúa de Jenaro de la Fuente
Domínguez, Santiago de Compostela, 15782, A Coruña, Spain*

^f*Departamento de Electrónica e Computación, Universidade de Santiago de Compostela, Rúa Lope Gómez de Marzoa, Santiago de
Compostela, 15782, A Coruña, Spain*

Abstract

1 Laser scanning is an active remote sensing technique applied in many disciplines to acquire state-of-the-art spatial
2 measurements. Semantic labeling is often necessary to extract information from the raw point cloud. Deep learning
3 methods constitute a data-hungry solution for the semantic segmentation of point clouds. In this work, we investigate
4 the use of simulated laser scanning for training deep learning models, which are applied to real data subsequently.
5 We show that training a deep learning model purely on virtual laser scanning data can produce results comparable
6 to models trained on real data when evaluated on real data. For leaf-wood segmentation of trees, using the KPConv
7 model trained with virtual data achieves 93.7% overall accuracy, while the model trained on real data reaches 94.7%
8 overall accuracy. In urban contexts, a KPConv model trained on virtual data achieves 74.1% overall accuracy on real
9 validation data, while the model trained on real data achieves 82.4%. Our models outperform the state-of-the-art model
10 FSCT in terms of generalization to unseen real data as well as a baseline model trained on points randomly sampled
11 from the tree mesh surface. From our results, we conclude that the combination of laser scanning simulation and deep
12 learning is a cost-effective alternative to real data acquisition and manual labeling in the domain of geospatial point
13 cloud analysis. The strengths of this approach are that a) a large amount of diverse laser scanning training data can
14 be generated quickly and without the need for expensive equipment, b) the simulation configurations can be adapted
15 so that the virtual training data have similar characteristics to the targeted real data, and c) the whole workflow can be
16 automated through procedural scene generation.

Keywords: Virtual Laser Scanning, LiDAR simulation, Point clouds, Machine Learning, Point-wise classification, Leaf-wood segmentation

1. Introduction

Light Detection and Ranging (LiDAR) can be used for three-dimensional (3D) observation of various environments, making it one of the most important geospatial data acquisition technologies (Shan and Toth, 2018). Point clouds are the main representation of LiDAR measurements. They have unstructured Euclidean data (geometric data) defining the spatial coordinates of the points (Otepka et al., 2013) and may include other data such as radiometric or backscatter features. Typically, the raw point clouds need to be segmented or classified in order to extract meaningful geoinformation or perform further analysis.

Virtual Laser Scanning (VLS) simulates laser scanning to generate virtual point clouds (Winiwarter et al., 2022; Dosovitskiy et al., 2017; Gastellu-Etchegorry et al., 2016), also called simulated or synthetic point clouds in other studies. In this work, we compare the performance of deep learning models trained with real-world and virtually scanned and thereby labeled point clouds. While there is a growing interest in deep learning on 3D point clouds, manual labeling is an extremely time-consuming task and is the main bottleneck in this area (Griffiths and Boehm, 2019).

We use VLS to generate perfectly annotated virtual point clouds from 3D scenes in a time and cost-efficient way to train deep learning models that generalize to real data. The 3D scenes for VLS can be manually designed, often made available in public 3D model repositories, derived from real data acquired with different sensors (e.g., LiDAR or photogrammetry), or computed through procedural scene generation algorithms (Zahs et al., 2023). Thus, VLS can be used to a) create huge and diverse synthetic datasets, b) generate targeted training data for critical classes or mimic the characteristics of a real dataset by modifying the scene, platform, and scanner configuration with little effort, and c) provide perfectly annotated datasets by transferring labels from the 3D scene with no need for point cloud annotation or real data acquisition.

Our experiments focus on two common point-wise point cloud classification problems: 1) semantic segmentation of urban scenes (Kölle et al., 2021) and 2) leaf-wood segmentation of trees (Ferrara et al., 2018; Krisanski et al., 2021b; Han and Sánchez-Azofeifa, 2022). For 1), we selected the mesh model of the Hessigheim3D urban benchmark dataset (Kölle et al., 2021) to create the virtual scene for VLS. For 2), we use computer-generated tree models for a fully virtual scene and the Wytham Woods 3D forest scene, which was reconstructed from real data (Calders et al., 2018; Liu et al., 2022).

Our objectives are to:

*Corresponding author at: Heidelberg University Institute of Geography, Im Neuenheimer Feld 368, 69120 Heidelberg, Germany *Email address:* hoefle@uni-heidelberg.de

- 45 1. Develop a theoretical definition of the Virtual Laser Scanning meets Deep Learning (VLS-DL) model.
- 46 2. Empirically validate the VLS-DL model using state-of-the-art data and algorithms to train deep learning models
47 on virtual point clouds that generalize to real point clouds.
- 48 3. Obtain proof-of-concept by applying the VLS-DL model to prominent and representative classification tasks
49 covering natural and urban environments.

50 In doing so, the following research questions will be answered:

- 51 1. To what degree do deep learning models trained with virtual laser scanning data generalize to real point clouds?
- 52 2. What are the quantitative differences between fitting a DL model to virtual or real-world point clouds?
- 53 3. What is the quantitative difference between using VLS-DL with meshes derived from real point clouds com-
54 pared to fully computer-generated scenes?

55 **2. Related work**

56 *2.1. Labeled datasets*

57 Several open-access labeled point cloud datasets in the literature have been used for benchmarking (Guo et al.,
58 2021). Most of them are from indoor or urban scenes. For instance, the widely used Stanford 3D Indoor Scene Dataset
59 (S3DIS) (Armeni et al., 2016) and the outdoor Semantic3D dataset (Hackel et al., 2017) were acquired using static
60 terrestrial laser scanning (TLS). Point clouds are also acquired with airborne platforms such as the DALES objects
61 dataset covering ground, vegetation, vehicles, buildings, fences, and powerlines (Singer and Asari, 2021). Some state-
62 of-the-art datasets, such as the KITTI 3D Object Detection benchmark (Geiger et al., 2012), are specifically oriented
63 to robotics, which combines high-resolution video cameras and laser scanning.

64 While the availability of high-quality labeled datasets is increasing, they are still limited, e.g., to certain geographic
65 regions, specific sensor systems, or specific objects (e.g., tree species). Annotating laser scanning point clouds manu-
66 ally is a cumbersome, time-consuming, and labor-intensive task. On top of that, interpreter bias and imperfect human
67 annotation often cause label noise (Kölle et al., 2021; Hackel et al., 2016), especially for fine-scale structures and in
68 partly occluded areas.

69 The outdoor Hessigheim benchmark (Kölle et al., 2021), which we use in our study, is a particularly interesting
70 labeled point cloud dataset for three reasons: 1) Acquired using an unoccupied aerial vehicle (UAV), it has a high
71 point density of about 800 pts/m² and achieves state-of-the-art representation of fine-grain features and also vertical
72 elements, 2) it covers eleven different classes in the broader categories ground, buildings, vegetation and urban objects,
73 and 3) it contains multiple epochs, captured in different seasons in 2018 and 2019. There is an online benchmark with
74 many results for the March 2018 epoch comparing some well-known models (Gao et al., 2022; Qi et al., 2017b;
75 Thomas et al., 2019)¹. Moreover, the Hessigheim 3D (H3D) dataset also includes annotated 3D meshes derived by

¹Accessed on 7 March 2023 (<https://ifpwww.ifp.uni-stuttgart.de/benchmark/hessigheim/results.aspx>).

76 combining the point cloud and oblique images. Table 1 represents the point-wise classification distribution of the
 77 different epochs, split into training and validation by the benchmark organizers.

Table 1: Percentage of points per class for the Hessigheim datasets. The classes from left to right are low vegetation (C00), impervious surface (C01), vehicle (C02), urban furniture (C03), roof (C04), facade (C05), shrub (C06), tree (C07), soil/gravel (C08), vertical surface (C09), and chimney (C10).

Dataset	Point-wise class distribution percentage (%)										
	C00	C01	C02	C03	C04	C05	C06	C07	C08	C09	C10
March 2018 (training)	35.96	17.53	0.43	1.95	10.56	2.02	1.81	13.60	14.45	1.64	0.04
March 2018 (validation)	25.85	22.21	1.27	3.15	21.10	3.82	2.36	15.34	4.10	0.70	0.11
March 2019 (training)	36.67	18.42	0.71	1.57	19.21	2.63	4.61	14.03	0.85	1.20	0.10
March 2019 (validation)	27.45	18.99	1.18	2.85	26.92	4.27	5.49	10.79	0.99	0.93	0.15

78 For the case of leaf-wood separation, Vicari et al. (2019) have published the real-world and virtual validation
 79 data (Boni Vicari et al., 2018a,b) for their Python library TLSeparation (14 trees in total). Wang et al. (2020) provided
 80 the 61 labeled tree point clouds from Momo Takoudjou et al. (2018), which they used for validation of the automatic
 81 leaf-wood segmentation tool LeWoS (Wang et al., 2021). The labeled Quantitative Structure Models (QSMs) obtained
 82 from point clouds of the Wytham Woods research forest (Oxfordshire, UK) used by Calders et al. (2018) and Liu et al.
 83 (2022) to model radiative transfer in forest stands have also been made openly available. We use the Wytham Woods
 84 dataset for VLS-based model training for leaf-wood classification. The main real-world leaf-wood dataset for our
 85 experiments consists of 11 TLS point clouds of different species, which have been manually labeled (Weiser et al.,
 86 2023). The tree point clouds have between 500,000 and 10,600,000 points and there are always more leaf points than
 87 wood points. Furthermore, we apply our models to two additional datasets from the literature to investigate how the
 88 models generalize. Appendix B contains a detailed description on the real-world training and validation point cloud
 89 datasets.

90 We are considering two types of leaf-wood experiments: isolated and near trees (Appendix A.2, Appendix B).
 91 For the “leaf-wood isolated” case, the trees are placed isolated from each other such that any input neighborhood for
 92 the deep learning model will contain points from a single tree. In the “leaf-wood near” case, the trees are close to each
 93 other, so their crowns overlap. Consequently, input neighborhoods potentially contain points from different trees.

94 2.2. Deep learning on point clouds

95 The PointNet model is generally accepted as the first relevant milestone of deep learning applied to point clouds
 96 because it achieved permutation invariance concerning input data while capturing the local structure of neighbor-
 97 hoods (Qi et al., 2017a). It was later extended to the PointNet++ model, which achieves hierarchical feature ex-
 98 traction similar to typical convolutional neural networks (CNN) following an incremental multiscale approach (Qi

99 et al., 2017b). There are also extensions of PointNet++, such as alsNet, which uses a batching framework strategy
100 to process vast airborne laser scanning (ALS) point clouds (Winiwarter et al., 2019). Other models, such as Kernel
101 Point Convolution (KPCConv), define the kernel as a finite set of points in the Euclidean space and a convolution oper-
102 ator based on a linear correlation where the distance between the kernel’s points and the input neighborhood’s points
103 weights the contribution of each particular point to the extracted feature (Thomas et al., 2019). Other deep learning
104 proposals aim to solve the problem of point clouds being unstructured data spaces without topological information
105 by estimating the implicit topology to improve the representation capabilities of raw point clouds. For instance, the
106 Dynamic Graph Convolutional Neural Network (DGCNN) model uses a convolutional operator on the graph’s edges
107 representing a local neighborhood updated from layer to layer (Wang et al., 2019). Furthermore, there are models
108 based on the sparse 3D convolutional neural networks introduced by Graham (2015). The main idea is to mitigate
109 the dimensionality curse that arises when generalizing discrete 2D convolutions to 3D by using a hash table where
110 the keys correspond to non-empty spatial locations, and the values are the index of the associated row in the input
111 matrix. These sparse convolutional models have been successfully applied to point-wise semantic segmentation of
112 point clouds (Graham et al., 2018; Schmohl and Sörgel, 2019).

113 The PointNet++ model has been modified to support 20,000 instead of 1,024 points per sample to achieve sensor
114 agnostic segmentation in forest point clouds (Krisanski et al., 2021b). This PointNet++-like model is part of the For-
115 est Structural Complexity Tool (FSCT), which we also use in our work to compare virtual-to-real generalization with
116 real-to-real generalization for leaf-wood segmentation (Krisanski et al., 2021a). Other works use a point-wise CNN to
117 segment stems from leaves, e.g., to study maize plants from terrestrial LiDAR point clouds (Ao et al., 2022). Some ap-
118 proaches combine geometric features with corrected optical features and achieve 96.20% and 94.98% overall accuracy
119 (OA) when performing leaf-wood segmentation on broadleaf and coniferous plants, respectively, and with an 84.26%
120 OA on mixed vegetation contexts (Wu et al., 2020). The leaf-wood segmentation problem has also been approached
121 as a time series problem comparing CNN, Long Short-Term Memory convolutional neural networks (LSTM CNN),
122 and Residual Network (ResNet) models (Han and Sánchez-Azofeifa, 2022). Recent works are thoroughly studying
123 the performance of PointNet++ for leaf-wood-flower segmentation depending on the number of scan positions and
124 the amount of noise (Rousseau et al., 2022).

125 2.3. *Virtual laser scanning*

126 The high cost and inherent errors of point cloud annotation suggest exploring VLS as an alternative or complement
127 to real data. There are software solutions to compute laser scanning simulations covering different scanner and scene
128 configurations. For instance, the Blender Sensor Simulation Toolbox (BlenSor) modified Blender (Blender Online
129 Community, 2023) to support casting many simultaneous rays, making it an efficient unified VLS and scene modeling
130 framework (Gschwandtner et al., 2011). Recent studies used laser scanning simulations within Blender to create train-
131 ing data for machine learning on 3D point clouds. For instance, Hildebrand et al. (2022) worked on the classification
132 of indoor scenes (like office and apartment rooms). However, for virtual point cloud data of larger outdoor scenes,

133 simulations have to be physically more sophisticated, i.e., taking into account beam divergence, multiple returns, and
134 complex sensors while handling large scenes and high simulated pulse frequencies. Blender-based solutions inherit
135 the modeling and performance limitations from software oriented to 3D animation, visual effects, video games, and
136 many more. We argue that obtaining the best VLS results demands specific VLS-oriented software. Consequently, we
137 decided to use the general-purpose high-performance Heidelberg LiDAR Operations Simulator HELIOS++ (Wini-
138 warter et al., 2022), to study its potential for successfully training deep learning models solely from virtual data. This
139 software supports many input formats, such as triangle meshes, voxels, geographic tagged images (GeoTIFF) as raster
140 models, and point clouds. Besides, it supports detailed XML specifications for different platforms and scanners. In-
141 stead of a ray tracing implementation similar to the native ray tracing of computer games such as Grand Theft Auto V
142 (GTA V) and 3D graphics software such as Blender, HELIOS++ provides an efficient object-aware ray tracing algo-
143 rithm that supports the high-performance parallel computation of different physical models on the light ray (Esmorís
144 et al., 2022).

145 There has been some previous work using synthetic data to train DL models. Hurl et al. (2019) achieve a 5%
146 improvement in average precision when using the Precise Synthetic Image and LiDAR (PreSIL) dataset to pre-train
147 object detection models validated against the KITTI 3D Object Detection benchmark (Geiger et al., 2012). The
148 PreSIL dataset includes point clouds generated from GTA V virtual scenes. It uses an alternative to classical ray
149 casting based on projecting the rays on an image plane to compute a depth interpolation that leads to more accurate
150 object representations. Others have implemented an in-game LiDAR in GTA V to generate virtual 3D point clouds
151 and improve the performance of CNN-like models at point-wise semantic segmentation. Enriching real data with
152 virtual data boosted classification intersection over union (IoU) on real validation data by around 8.9% (Wu et al.,
153 2018). Furthermore, Bryson et al. (2023) explored a variant of leaf-wood segmentation using virtual data to train a
154 deep learning model based on the PointNet++ architecture. Instead of typical leaf and wood classes, they considered
155 stem (main tree stem and large branches) and foliage (canopy and small branches). They found that models trained on
156 virtual data can outperform models trained on real data when there are not enough labeled real point clouds to achieve
157 convergence. However, with abundant real data, models trained on real data outperform those trained on virtual data.

158 **3. Method**

159 Central to our approach is the combination of virtual laser scanning (VLS) and deep learning (DL) for point cloud
160 semantic segmentation. In this section, we first consider the main theoretical components of VLS and DL applied to
161 point clouds. We then present our experimental framework, where we train our deep learning model with a) only real
162 data and b) only VLS data and then evaluate the performance by predicting class labels on a withheld validation set
163 of the real data. The whole workflow is illustrated in Figure 1. We provide a detailed description of the virtual scene
164 modeling and the simulated platform and scanner in Appendix A and the real training and validation point clouds in
165 Appendix B.

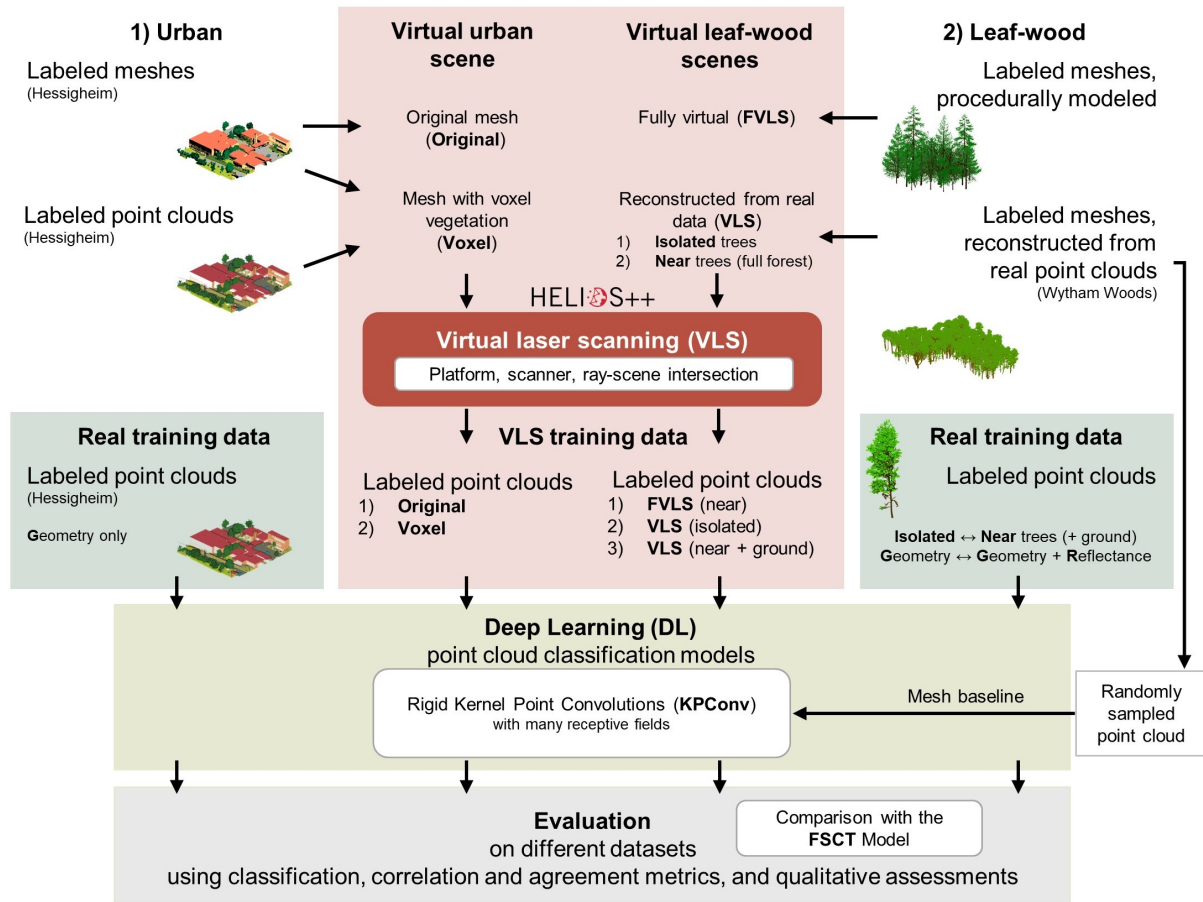


Figure 1: The workflow summarizes the entire experimental framework. The top shows the generation of 3D scenes, which are virtually scanned with HELIOS++ to create virtual labeled point clouds for training the VLS-DL models for 1) urban classification and 2) leaf-wood classification. For the urban case, meshes and point clouds from the Hessigheim3D dataset (Kölle et al., 2021) are used. For the leaf-wood case, synthetic meshes generated with the algorithm by Weber and Penn (1995), and the Wytham Woods 3D model (Calders et al., 2018; Liu et al., 2022) are used. Real labeled point clouds (Hessigheim for the urban case, point clouds from Weiser et al. (2023) for the leaf-wood case) serve as training data for the deep learning (DL) models. The performance of the models trained on real data and those trained on virtual data are evaluated and compared quantitatively and qualitatively. The leaf-wood models are also compared with the FSCT model (Krisanski et al., 2021a) and a mesh sampling baseline model.

166 *3.1. Theoretical model*

167 The theoretical VLS-DL model illustrates the key components of a virtually trainable model based on connecting
 168 simulation and deep learning. In this section, we describe the many submodels and how they are connected from the
 169 first (parametric ray generation) to the last (neural network).

170 The VLS-DL model on a 3D Euclidean space starts by simulating a trajectory using a parametric model (Stewart,
 171 2012) with position $(x_1(t), x_2(t), x_3(t))$ and associated direction $(\varphi_1(t), \varphi_2(t), \varphi_3(t))$. A ray is defined from an origin
 172 point \mathbf{o}_i and an associated director vector \mathbf{v}_i such that $\{\mathbf{o}_i + t\mathbf{v}_i : t \geq 0\}$ (Boyd and Vandenberghe, 2004). However, for
 173 VLS, the travel time of the ray is used to estimate the distance. Consequently, a ray in VLS context must be defined
 174 as $\{\mathbf{o}_i + t\mathbf{v}_i : t \geq \epsilon\}$, where $\epsilon \in \mathbb{R}_{>0}$ is the minimum distance threshold defining the scanner. Thus, it is possible to
 175 express the finite set of rays in the simulation such that $r_i = \{\mathbf{o}_i = o[t_i, x_1(t_i), \dots, \varphi_3(t_i)], \mathbf{v}_i = v[t_i, x_1(t_i), \dots, \varphi_3(t_i)]\}$,
 176 where o and v map the parametric model to the final ray. These maps can be as simple as the identity function or as
 177 complicated as the composition of many reference systems mixed with non-linear deflection models.

178 Let V be a finite set of points in \mathbb{R}^3 that lie on a common plane where they define a convex polygon. This convex
 179 polygon can be seen as the feasible region of a linear programming problem (LP) (Solow, 2014). Moreover, as the
 180 objective function is null, any solution is optimal, which means the LP can be seen as a feasibility problem. Let
 181 $\mathbf{V} \in \mathbb{R}^{2 \times |V|}$ be the matrix representing the vertices in V on the local coordinates of their plane. Since each convex
 182 polygon is a convex set, any convex combination of its vertices $\sum_j^{|V|} \lambda_j \mathbf{v}_{*j}$ satisfying $\sum_j^{|V|} \lambda_j = 1$ and $\lambda_j \geq 0$ will be
 183 inside the polygon (Boyd and Vandenberghe, 2004), where \mathbf{v}_{*j} is the row j of matrix \mathbf{V} . The convex combination of
 184 the vertices of a convex polygon is illustrated on the left side of Figure 2, while the finite set of feasible regions is
 185 illustrated on the right side. Any scene point \mathbf{p} must belong to the plane defined by a set of vertices V_i and lie inside
 186 a feasible region when expressed as the point \mathbf{q} in the local coordinates of this plane. Then, all scene points can be
 187 modeled as belonging to the union of a finite set of planes π_i constrained by linear systems $\mathbf{V}'_i \boldsymbol{\lambda}_i = \mathbf{q}'$ subject to $\boldsymbol{\lambda}_i \geq 0$.
 188 Note for any polygon defined by the vertices V_i the constraint $\sum_j^{|V_i|} (\boldsymbol{\lambda}_i)_j = 1$ is implicit on the definition of \mathbf{V}'_i and \mathbf{q}'
 189 given in Equation 1, both expanded with ones.

$$\mathbf{V}'_i = \begin{bmatrix} \mathbf{V}_i \\ \mathbf{1}^\top \end{bmatrix}, \mathbf{q}' = \begin{bmatrix} \mathbf{q} \\ 1 \end{bmatrix} \quad (1)$$

190 To conclude the VLS model, note that the feasible regions contain infinite points, but the amount of rays is finite.
 191 Thus, the intersection between the rays and the feasible regions leads to a finite set of points constituting the baseline
 192 solution of the ray tracing VLS model. The final output point set P generated through VLS can be defined as the set
 193 of points that satisfy all the constraints given in Equation 2. In this equation, each $\psi_k \leq \tau_k$ stands for each of the
 194 K non-necessarily linear filters. These filters can be physical-based (e.g., $-\psi_k$ is the power of the reflected light at
 195 the sensor and $-\tau_k$ is the minimum power the sensor can detect) or simulation conveniences (e.g., ψ_k is the distance
 196 between origin and target points and τ_k is an arbitrary maximum distance threshold). The input vector $\boldsymbol{\theta}$ represents
 197 other potential simulation parameters (e.g., the wavelength).

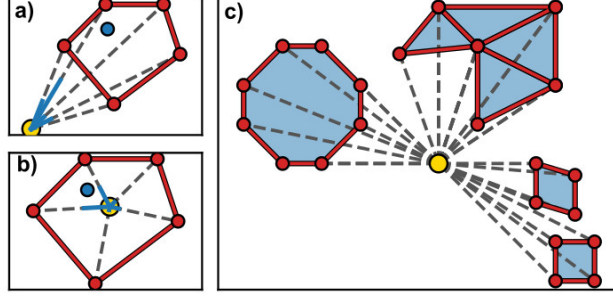


Figure 2: The left side figures a) and b) show how a point (blue) inside a convex set can be expressed as a convex combination of its vertices (red) understood as vectors (gray) from the origin (yellow). Note that the blue highlighted segments represent the magnitude of displacement on the vector for the convex combination. The right figure c) shows that many intersections of halfspaces can be seen as many different linear feasible regions (blue) representing a linear system each.

$$P = \left\{ \mathbf{p} \in \mathbb{R}^3 : \begin{array}{l} \mathbf{p} = \mathbf{o}_j + t\mathbf{v}_j \in \pi_i, \quad t \geq \epsilon, \\ \mathbf{V}'_i \boldsymbol{\lambda}_i = \mathbf{q}', \quad \boldsymbol{\lambda}_i \geq 0, \\ \bigwedge_k^K \psi_k(\mathbf{p}, \pi_i, \mathbf{r}_j, t, \boldsymbol{\theta}) \leq \tau_k \end{array} \right\} \quad (2)$$

198 From now on, the matrix $\mathbf{P} = [\mathbf{X} | \mathbf{F} | \mathbf{y}] \in \mathbb{R}^{m \times 5}$ will refer to the output point cloud of m points generated with
 199 VLS where $\mathbf{X} \in \mathbb{R}^{m \times 3}$ represents the simulated geometric data, $\mathbf{F} \in \mathbb{R}^{m \times 1}$ is a column-vector matrix of ones to enable
 200 feature extraction with deep learning, and $\mathbf{y} \in \mathbb{Z}^{m \times 1}$ is a column-vector such that y_i is an integer representing the class
 201 to which the i -th point belongs. This matrix \mathbf{P} can also be seen as the input to a fitting algorithm where a loss function
 202 \mathcal{L} is defined for an estimator $\hat{\mathbf{y}}(\mathbf{X}, \mathbf{F}; \boldsymbol{\omega})$ that uses the parameters $\boldsymbol{\omega}$ to predict the class. Since deep-learning models are
 203 based on gradient descent-like optimization methods (Zhang, 2017; Goodfellow et al., 2016), the VLS-DL model can
 204 be summarized as Equation 3, where α represents the learning rate. Before adventuring forth, it is worth mentioning
 205 that the proposed training data generation where $\mathbf{y} \in \mathbb{Z}^m$ can be easily adapted to regression problems where $\mathbf{y} \in \mathbb{R}^m$
 206 (e.g., \mathbf{y} can be a point-wise surface roughness metric).

$$\boldsymbol{\omega}_{t+1} = \boldsymbol{\omega}_t - \alpha \nabla_{\boldsymbol{\omega}_t} \mathcal{L}(\mathbf{P}; \boldsymbol{\omega}_t) \quad (3)$$

207 Deep learning applied to point clouds often requires a domain-specific operator for feature extraction. For exam-
 208 ple, it is possible to address this issue using the Kernel-Point Convolution (KPCConv) operator (Thomas et al., 2019)
 209 as the feature extraction method for the estimator $\hat{\mathbf{y}}$.

210 First, let $\mathcal{Q} = \{\mathbf{Q} \in \mathbb{R}^{K \times 3}, \mathbf{W}_1, \dots, \mathbf{W}_K \in \mathbb{R}^{D_{\text{IN}} \times D_{\text{OUT}}}\}$ represent a kernel of K points (regularly distributed by
 211 solving an energy minimization problem) at a given layer that maps D_{IN} input features to D_{OUT} output features.
 212 For then, any point from the geometric data $\mathbf{x}_{i^*} \in \mathbb{R}^3$ can be convolved considering its neighborhood $\mathcal{N}_{\mathbf{x}_{i^*}}$, e.g.,
 213 $\mathcal{N}_{\mathbf{x}_{i^*}} = \{\mathbf{x}_{j^*} : \|\mathbf{x}_{j^*} - \mathbf{x}_{i^*}\| \leq r\}$ (where r is the radius). The rigid KPCConv operator based on linear correlation is for-
 214 mally described in Equation 4. In this equation, \mathbf{q}_{k^*} are the points defining the kernel in the Euclidean space, i.e., rows

215 from the \mathbf{Q} matrix, the \mathbf{W}_k matrices are the weights for each kernel point, the \mathbf{f}_{j^*} vector is the j -th row of the input
 216 features matrix \mathbf{F} , and σ defines the influence distance.

$$(\mathbf{P} * \mathbf{Q})(\mathbf{x}_{i^*}) = \sum_{\mathbf{x}_{j^*} \in \mathcal{N}_{\mathbf{x}_{i^*}}} \sum_{k=1}^K \max \left\{ 0, 1 - \frac{\|\mathbf{x}_{j^*} - \mathbf{x}_{i^*} - \mathbf{q}_{k^*}\|}{\sigma} \right\} \mathbf{W}_k \mathbf{f}_{j^*} \quad (4)$$

217 3.2. Experimental framework

218 Our experiments shall be representative of many topographic applications and thus cover urban (Hessigheim) and
 219 natural (leaf-wood) contexts for which real data is available. We generate virtual point clouds for those contexts using
 220 the VLS software HELIOS++ and assess the performance of deep learning-based semantic segmentation using real or
 221 virtual data for the training. We also train models using real data with reflectance for the leaf-wood segmentation cases
 222 to compare them with the real and virtual models using only geometric data. For evaluation, we use classification
 223 quality assessment metrics, correlation and agreement metrics, expert-based evaluation, and a comparison with a
 224 model trained from randomly sampled points from the scene meshes. Moreover, we compare the virtual-to-real
 225 generalization of our VLS-DL model with the real-to-real generalization of the FSCT model (Krisanski et al., 2021a)
 226 (Figure 1).

227 We specialize our VLS-DL model to work with geometric data. Signal strength-related features are discarded
 228 because they are not well-standardized for all sensors and are more difficult to compare (Höfle and Pfeifer, 2007;
 229 Jutzi and Gross, 2009; Wang et al., 2015). We use the grid subsampling strategy proposed in the original KPConv
 230 paper (Thomas et al., 2019) to explore the resolution from the deep learning model perspective.

231 3.2.1. Virtual laser scanning

232 For the urban classification experiments, we use virtual 3D scenes reconstructed from real 3D data, namely from
 233 UAV-borne point clouds and imagery of Hessigheim. Two versions of the virtual Hessigheim scene (Kölle et al., 2021)
 234 are created (Table 2). The first version directly uses the original labeled meshes from the Hessigheim 3D benchmark.
 235 For the second version, the Hessigheim mesh is modified by replacing mesh faces labeled as the vegetation classes
 236 with voxel models created from the Hessigheim3D point cloud (Table 2). Our hypothesis is that voxels, if using an
 237 appropriate voxel size, are an adequate object representation and lead to better classification performance because the
 238 virtual rays can penetrate through gaps in the vegetation (Weiser et al., 2021). We use the same training and validation
 239 split as in the Hessigheim 3D benchmark.

240 Separate materials are assigned to the different classes through material library files (MTL). We exploit the
 241 HELIOS++ functionality of assigning integer class IDs to the materials by adding the custom *helios_classification*
 242 attribute (Winiwarer et al., 2022). In the simulation, the class labels are then transferred from the object intersected
 243 by the virtual ray to the point created through the intersection. In the case of multiple intersections, each one will lead
 244 to a point with a class coming from the respective intersected object.

245 With our experiments of leaf-wood classification, we cover two central ways to generate virtual scenes, namely 1)
246 with procedural 3D modeling, where objects are fully computer generated, and 2) by reconstructing real scenes from
247 high-resolution real-world measurements. We refer to point clouds we simulate with the resulting datasets as 1) fully
248 virtual laser scanning (FVLS) and 2) VLS.

249 For the fully synthetic scenes, 30 tree models with different leaf and needle shapes are generated using the algo-
250 rithm of Weber and Penn (1995) with different parameter sets. All trees are arranged in a small forest stand, with their
251 crowns clearly overlapping.

252 For the scenes reconstructed from real data, we use the synthetic Wytham Woods scene of quantitative structure
253 models (QSMs) provided by Calders et al. (2018) and Liu et al. (2022)².

254 We create two versions of the virtual Wytham Woods scene, one with selected isolated trees and one with the full
255 forest plot (closely spaced or "near" trees) (Table 2). The full Wytham Woods forest scene is spatially divided into
256 training and validation.

257 Two different 3D parametric platforms and scanner models are used for the laser scanning simulations of the
258 different scenes.

259 For the Hessigheim simulations, we use a model of the *RIEGL VUX-1LR* scanner (RIEGL Laser Measurement
260 Systems, 2022) and similar acquisition settings as in the Hessigheim March 2018 epoch (Cramer et al., 2018). These
261 are summarized in Table A.9 of Appendix A.1. The parametric model linearly approximates the real trajectory,
262 assuming a constant speed of 8 m/s. The o map transforms the point position by composing the platform and the
263 scanner's reference systems. The v map transforms the direction considering the scanner head expressed in the plat-
264 form's local reference system, where a rotating mirror deflection model is solved at each simulation step to determine
265 the ray's direction.

266 The 3D tree scenes for leaf-wood classification are scanned with multiple scan positions using a model of the
267 *RIEGL VZ-400 TLS* (RIEGL Laser Measurement Systems, 2017) and similar scan settings as used in the validation
268 dataset (Table A.10 in Appendix A.2). Since these are tripod-based simulations, any $x_i(t)$ and $\varphi_i(t)$ functions are
269 constants representing the tripod's static position. The o map is the identity function, while the v map directly solves
270 a polygon mirror deflection model matching the scanner specification.

271 The process of virtual scene generation and virtual laser scanning for both the urban and the leaf-wood experiments
272 is described in detail in Appendix A.

273 Finally, a point cloud obtained by sampling points from the mesh surface is also generated for the near trees
274 leaf-wood case (full Wytham Woods forest stand) to quantify the extent to which VLS contributes to better feature
275 extraction on the DL side. The resulting training dataset has 69,999,073 points, which is slightly higher but similar to
276 the 63,297,807 points we use for training with VLS point clouds merged from different scan positions. This dataset is

²https://bitbucket.org/tree_research/wytham_woods_3d_model/src/add_dart/DART_models/ (Accessed on 19 October 2022)

Table 2: Description of the virtual scenes used in the HELIOS++ laser scanning simulations for the leaf-wood classification and the urban classification use cases.

Leaf-wood classification	
<hr/>	
(1) Fully Virtual Forest Stand	Up to 30 tree models are created using the algorithm by Weber and Penn (1995) and arranged into a forest stand with overlapping crowns.
(2) Reconstructed Virtual Forest Stand	The full Wytham Woods 3D forest model is used: Trees are closely spaced, their crowns are overlapping and terrain in the form of a meshed digital terrain model is included.
(3) Reconstructed Isolated Trees	Six synthetic datasets are used, each by manually placing eight randomly selected 3D tree models from the Wytham Woods dataset in a circular plot. Each tree is isolated, and the tree crowns do not overlap.
<hr/>	
Urban scene classification - Hessigheim	
<hr/>	
(1) Original Mesh	The original Hessigheim3D mesh is used as the 3D VLS scene.
(2) Modified mesh with voxel vegetation	Vegetation (Shrub and Tree classes) are removed from the Hessigheim 3D mesh and modeled from the point clouds using small voxels ($5\text{ cm} \times 5\text{ cm} \times 5\text{ cm}$). Furthermore, the surface below the vegetation is reconstruction to prevent holes. The resulting hybrid mesh-voxel model serves as the 3D VLS scene.
<hr/>	

277 used to train the baseline Mesh-DL model.

278 3.2.2. Deep learning

279 For the details regarding the KPConv network architecture, we would like to refer to Thomas et al. (2019). In the
280 following, we focus on the main particularities characterizing this work.

281 First, we explain our training procedure. It consists of training a model for a fixed number of epochs, then using
282 the model to classify validation data that has not been seen before and repeating until a maximum number of training
283 processes has been reached. Each training process draws a different randomly selected set of neighborhood centers
284 for training. We use the evaluations on validation data to assess training evolution and compare virtual training with
285 real training exhaustively.

286 Instead of using an exponential learning rate decay as usually done with KPConv models (Thomas et al., 2019; de
287 Gélis et al., 2023), we use a combination of early stopping and reducing learning rate on the plateau. We do this to
288 decrease our learning rate smoothly on demand for each training process instead of a priori deciding on a fixed number

289 of epochs for the learning rate decay. More concretely, we monitor the sparse categorical cross-entropy loss function
290 with 50 epochs patience for the early stopping of a training process and reduce the learning rate multiplying by $10^{1/3}$
291 with 20 epochs patience and an additional 10 epochs cooldown for consecutive reductions. This configuration can
292 lead to dividing the learning rate by 10 for every hundred epochs, as in the original proposal, but it will only trigger
293 the reduction if the loss function reaches a plateau. The patience count for the learning rate reduction is preserved
294 among training processes. As in the original model, we use 400 epochs per training process for the Hessigheim3D
295 point clouds. We use 200 epochs for leaf-wood point clouds because they converge much faster. In both cases, we use
296 an initial learning rate of 10^{-3} .

297 For the experiments on real data that also use reflectance, we normalize all the reflectance values to lie inside the
298 $[0, 1]$ interval in a dataset-dependent way. Generalized approaches are impossible since intensity and reflectance often
299 change between datasets.

300 As in Thomas et al. (2019), we divide the large point clouds into small subclouds contained in spheres. We dis-
301 tribute the spheres along the scene with a regular spacing of 0.5 times the sphere radius. Separations greater than
302 $2/\sqrt{3}$ times the radius will lead to missing regions for 3D scenes. We selected 0.5 times because it is small enough
303 to increase classification overlapping (which increases reliability) but not too big to lead to intractable classifica-
304 tions. After classification, probabilities for points that appear in multiple spheres are averaged, and the class with the
305 maximum average probability is assigned.

306 3.2.3. Evaluation

307 The model evaluation metrics can be classified into aggregated metrics and per-class metrics. For the aggregated
308 metrics, we are computing the Overall Accuracy (OA) (Sokolova and Lapalme, 2009), the Jaccard score or Inter-
309 section over Union (IoU) (Jaccard, 1901), the multiclass Precision and Recall, the F1 score (Sokolova and Lapalme,
310 2009), the Matthews Correlation Coefficient (MCC) (Matthews, 1975), and Cohen’s Kappa score (Cohen, 1960). The
311 evaluation metrics can be categorized into classification quality assessment (e.g., OA and F1) and correlation and
312 agreement assessment (e.g., MCC and Kappa score). When aggregating the evaluation metrics, both the weighted and
313 unweighted averages are considered in a non-label-agnostic way to assess the models with and without accounting for
314 class imbalance. For a per-class evaluation, we compute the F1 scores, as used by Kölle et al. (2021) for evaluation of
315 the Hessigheim 3D benchmark. We also carry out an expert-based visual evaluation for the leaf-wood case.

316 Finally, we design a specific evaluation method to compare VLS-sensed point clouds with randomly sampled
317 points on the virtual leaf-wood mesh. For this evaluation, we consider the geometric features of linearity and pla-
318 narity (Weinmann et al., 2015; Hackel et al., 2016) to characterize a spherical neighborhood defined by a 5 cm radius.
319 Then, we can compare these quantitative features to analyze the difference between VLS and mesh sampling.

320 **4. Results**

321 In this section, we present the results of our experiments. We start with an aggregated comparison between models.
 322 Then, we provide detailed results for both the Hessigheim and the leaf-wood experiments. Finally, we present the
 323 results of the comparison between mesh sampling, VLS, and real-world point clouds.

324 *4.1. Aggregated comparison*

Table 3: Aggregated evaluation and agreement metrics for the Hessigheim datasets in March 2018 and March 2019. The KPConv model was trained with real or virtual data. There are two different VLS training datasets. One uses the original triangle mesh, and the other uses a hybrid scene with the original triangle mesh and voxels to represent vegetation. The metrics from left to right are Overall Accuracy (OA), Precision (P), Weighted Precision (WP), Recall (R), Weighted Recall (WR), mean Intersection over Union (mIoU), Weighted mean Intersection over Union (WIoU), F1 score (F1), Weighted F1 score (WF1), Matthews Correlation Coefficient (MCC), and Cohen’s Kappa score (K).

Train	Validation	Metrics (%)										
		OA	P	WP	R	WR	mIoU	WIoU	F1	WF1	MCC	K
VLS (mesh)	March 2018	66.1	44.5	70.4	57.1	66.1	33.6	51.9	46.4	67.1	58.4	58.1
VLS (voxel)	March 2018	74.1	52.3	78.5	67.4	74.1	42.6	63.0	55.2	75.7	68.0	67.7
Real	March 2018	82.4	72.9	79.9	59.2	82.4	51.0	71.0	63.1	80.5	78.2	78.0
VLS (mesh)	March 2019	63.9	44.8	64.1	38.1	64.0	28.0	49.0	39.0	63.6	54.8	54.7
VLS (voxel)	March 2019	74.4	47.8	76.1	64.6	74.4	39.1	62.3	50.4	75.0	67.9	67.7
Real	March 2019	81.4	54.7	82.4	66.1	81.4	46.0	71.3	57.9	81.7	76.6	76.6

325 We compared different versions of the KPConv model, varying the initial cell size for the grid subsampling, which
 326 defines the receptive field of the finest grain layers. Figure 3 shows a summary of these results for the Hessigheim
 327 datasets (a, b, c, d) and the near trees leaf-wood case (e, f, g, h). We used one more training process for the leaf-wood
 328 segmentation experiments because their training requires fewer epochs than semantic segmentation in urban contexts.

329 For both the March 2018 and the March 2019 real-world Hessigheim datasets, OAs above 80% and MCCs around
 330 75% were achieved. These scores derived with real data act as a baseline against which we evaluate the results of the
 331 VLS-DL model. While the OA of the VLS-DL model based on the original Hessigheim mesh data is only 66.1%, we
 332 can improve this value by 8% up to 74.1% by replacing the mesh representation of vegetation (C06: shrub and C07:
 333 tree) with a voxel model, which results in a more realistic synthetic point cloud for these classes. Larger initial cell
 334 sizes in the neural network work better for real and virtual Hessigheim point clouds. Small receptive fields (2 and
 335 3 cm) perform poorly in these datasets because they barely contain any information about the global context.

336 The best models from the Hessigheim experiments are compared in Table 3. For the geometric KPConv case,
 337 this is the model with an initial cell size of 9 cm, and for the virtual case, this is the model with an initial cell size of
 338 10 cm (Figure 3). Using the original mesh as the VLS input scene leads to a 16.3% lower OA for March 2018 and

Table 4: Aggregated evaluation and agreement metrics for the leaf-wood datasets with isolated and near trees, respectively. The KPCnv models (KPC) were trained with real or virtual data. The FSCT model (Krisanski et al., 2021a) is used to quantify the real-to-real generalization with a different model than ours. In the features column, G means geometric features, and R means reflectance. The VLS model is trained on point clouds simulated with meshes derived from real trees, while the FVLS model is trained on simulated point clouds of fully synthetic trees. The metrics from left to right are Overall Accuracy (OA), Precision (P), Weighted Precision (WP), Recall (R), Weighted Recall (WR), mean Intersection over Union (mIoU), Weighted mean Intersection over Union (WIoU), F1 score (F1), Weighted F1 score (WF1), Matthews Correlation Coefficient (MCC), and Cohen’s Kappa score (K).

Model	Features	Validation	Metrics (%)										
			OA	P	WP	R	WR	mIoU	WIoU	F1	WF1	MCC	K
FVLS KPC	G	Isolated	93.2	88.2	93.8	92.4	93.2	82.3	87.8	90.0	93.3	80.4	80.1
VLS KPC	G	Isolated	87.0	84.1	86.7	81.6	87.0	71.5	77.4	82.7	86.8	65.7	65.5
Real KPC	G	Isolated	93.5	93.2	93.5	88.5	93.5	83.1	87.8	90.5	93.3	81.5	81.1
Real KPC	G+R	Isolated	95.4	91.0	96.0	96.3	95.4	87.6	91.7	93.3	95.6	87.1	86.6
FSCT	G	Isolated	83.5	77.6	86.3	83.4	83.5	66.9	73.6	79.5	84.3	60.7	59.3
FVLS KPC	G	Near	92.6	87.4	92.7	87.8	92.6	78.8	86.9	87.6	92.7	75.2	75.2
VLS KPC	G	Near	93.7	91.0	93.5	87.0	93.7	80.6	88.4	88.8	93.5	77.8	77.6
Real KPC	G	Near	94.7	96.0	94.9	86.0	94.7	82.5	89.8	90.0	94.4	81.3	80.0
Real KPC	G+R	Near	94.8	94.8	94.8	87.0	94.8	83.0	90.0	90.3	94.5	81.4	80.7
FSCT	G	Near	88.7	80.3	89.5	83.9	88.7	70.9	81.1	81.9	89.0	64.1	63.9

339 17.5% lower OA for March 2019 compared to the real data. Improving the scene with voxels for vegetation reduces
340 this difference to 8.3% in OA for March 2018 and 7.0% for March 2019. Compared to the real geometric model, the
341 original mesh VLS-DL model results in an MCC reduction of 19.8% for March 2018 and 21.8% for March 2019.
342 With the virtual scene with voxels, the MCC reduction is about 10.2% for the March 2018 epoch and 8.7% for the
343 March 2019 epoch. These results indicate that improved scene modeling is fundamental for VLS-based multiclass
344 semantic segmentation in urban point clouds. There are no significant differences between March 2018 and March
345 2019 epochs.

346 For the leaf-wood datasets, Figure 3 shows that for real models, a smaller initial cell size (1 and 2 cm) works better
347 than a bigger one. These results suggest that fine-grain information is important to separate the wood components
348 (trunk and branches) from the leaves. However, VLS-DL models perform better on real datasets when trained on
349 bigger initial cell sizes (5 and 6 cm), while they perform better on virtual datasets with smaller cell sizes. These
350 results suggest that fine-grain vegetation modeling in the input scene might lead to even better VLS-DL models for
351 leaf-wood segmentation.

352 Table 4 presents a quantitative comparison between the best leaf-wood models (Geometric, Reflectance, VLS-DL,
353 and FVLS-DL) and the FSCT model (Krisanski et al., 2021a).

354 For the case of the isolated trees, the model trained on geometric data achieves only 0.3% more OA and 1.1%
 355 higher MCC than the FVLS-DL model, while considering reflectance leads to 2.2% greater OA and 6.5% greater
 356 MCC. The virtual-to-real generalization of the FVLS-DL model is 9.7% better in OA and 19.7% better in MCC than
 357 the real-to-real generalization of the FSCT model trained on a different dataset than ours (Krisanski et al., 2021a). For
 358 the near trees case, the real model trained on reflectance is not considerably better than the model trained on just the
 359 geometry. Here, the VLS-DL model (trained on the Wytham Woods synthetic point cloud) has higher accuracy than
 360 the FVLS-DL model, and achieves just 1% lower OA and 3.5% lower MCC than the real models.

361 4.2. Hessigheim results

Table 5: Evaluation of different submitted models on the test data from the Hessigheim3D benchmark (<https://ifpwww.ifp.uni-stuttgart.de/benchmark/hessigheim/results.aspx>). The aggregated metrics are overall accuracy and mean F1 score. The F1 score is also calculated on a per-class basis. The geometric KPConv and VLS-DL models are our real and virtual models. The classes from left to right are low vegetation (C00), impervious surface (C01), vehicle (C02), urban furniture (C03), roof (C04), facade (C05), shrub (C06), tree (C07), soil/gravel (C08), vertical surface (C09), and chimney (C10).

Model	OA (%)	F1 (%)	F1 per-class (%)										
			C00	C01	C02	C03	C04	C05	C06	C07	C08	C09	C10
WHU221118	89.8	79.0	92.9	90.2	78.5	57.9	95.7	80.4	68.5	97.2	62.4	73.1	72.5
Shi220705	84.2	63.5	87.6	85.6	52.4	36.7	95.5	69.3	47.4	94.3	25.1	66.0	38.6
Zhan221025	79.7	65.3	84.3	77.9	58.1	42.3	93.3	65.4	53.5	95.3	23.7	59.9	64.7
Gao-PN++210422	68.5	41.2	78.1	72.1	31.8	13.7	74.0	47.8	28.3	71.8	9.7	21.7	4.4
jjabin221114	58.3	43.4	66.2	18.0	34.2	38.0	72.0	69.0	47.7	78.7	9.8	35.9	8.3
VLS-DL	68.8	54.2	71.1	55.8	2.7	25.9	93.7	73.3	39.0	93.2	20.7	70.4	49.8
Geometric KPConv	81.7	63.8	84.8	82.0	19.5	42.4	94.8	77.8	59.1	94.5	3.6	73.8	69.2

362 We evaluated our models in detail on the Hessigheim3D (Kölle et al., 2021) public test benchmark. The results of
 363 the Hessigheim3D benchmark in Table 5 shows that our real models provide average results despite using geometric
 364 information only. While using real data leads to similar evaluation on validation and test, the VLS-DL model gener-
 365 alizes worse in the test dataset than in the validation dataset (12.9% decrease in OA compared to 8.3% decrease with
 366 validation data). However, it still provides results that match the performance of PointNet++-based models such as
 367 Gao-PN++210422 trained on real data.

368 Returning to the validation dataset, Table 6 offers the quantitative evaluation of our models on a per-class ba-
 369 sis. While low vegetation and impervious surfaces give acceptable results, all models have problems with soil/gravel
 370 points. This can be explained by the difficulty of distinguishing between types of ground points using geometric data
 371 only and no spectral/radiometric information. These results can also be analyzed in confusion matrices, shown in
 372 Figure 4 for the real geometric KPConv model and in Figure 5 for the VLS-DL model. The confusion matrices in

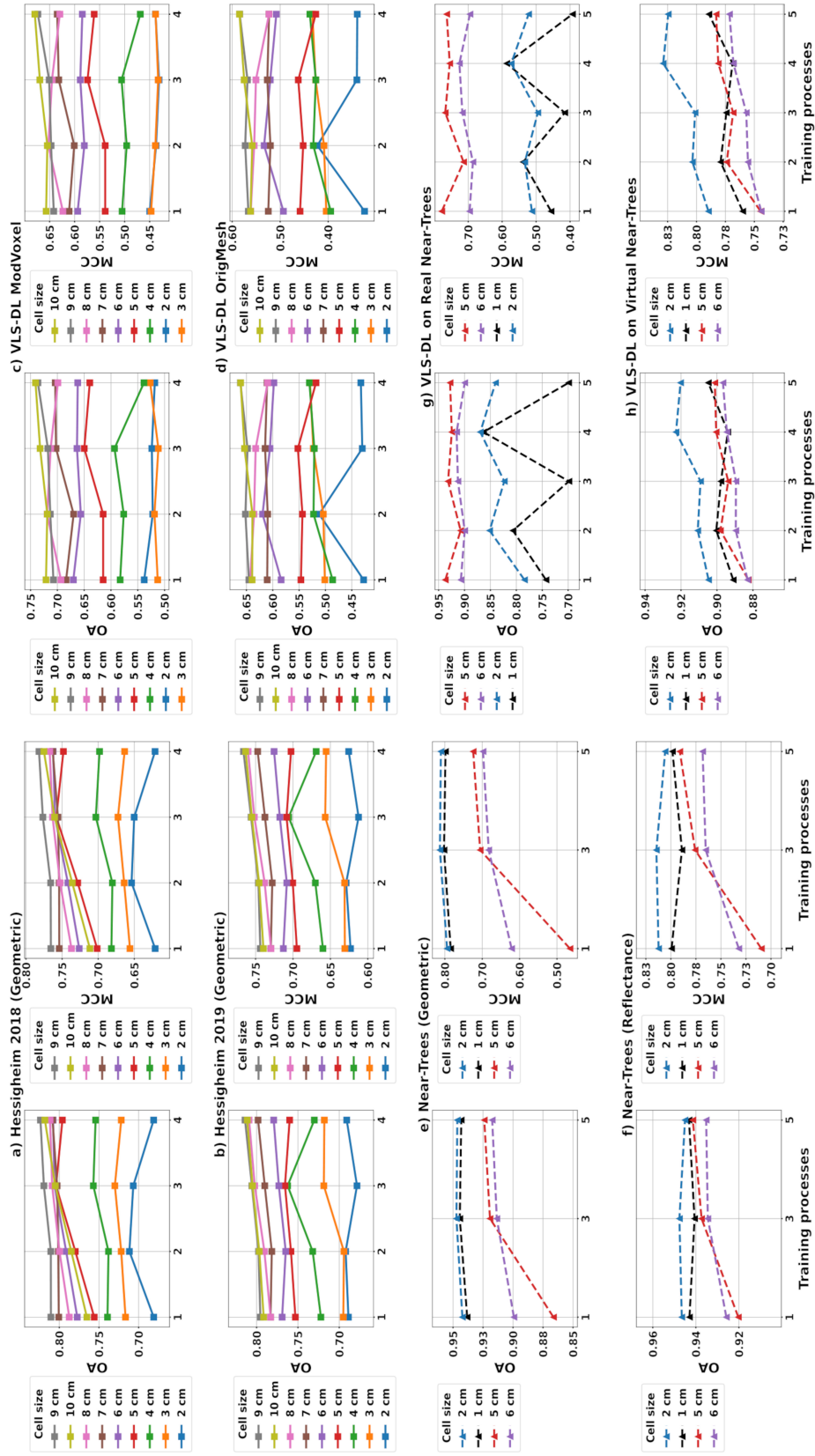


Figure 3: Comparison of many models with different initial cell size configurations leading to different receptive fields. For each model, the overall accuracy (OA) and the Matthews Correlation Coefficient (MCC) are plotted on the y-axis while the x-axis represents the number of training processes. Each training process picks a new sample of neighborhood centers. Solid line graphs refer to the Hessigheim datasets, while dashed line graphs refer to the leaf-wood dataset.

Table 6: Evaluation and agreement metrics per class for the Hessigheim datasets in March 2018 and March 2019. The real geometric KPConv model was trained with real data. There are two different VLS-DL models. One uses the original triangle mesh, and the other uses a hybrid scene with the original triangle mesh and voxels to represent vegetation. The classes from left to right are low vegetation (C00), impervious surface (C01), vehicle (C02), urban furniture (C03), roof (C04), facade (C05), shrub (C06), tree (C07), soil/gravel (C08), vertical surface (C09), and chimney (C10).

Model	Validation	F1 per-class (%)										
		C00	C01	C02	C03	C04	C05	C06	C07	C08	C09	C10
VLS-DL Original	March 2018	65.2	68.3	12.1	31.9	81.1	61.4	25.9	74.4	3.7	46.8	39.6
VLS-DL Voxel	March 2018	71.0	70.7	18.7	33.9	90.5	72.7	44.1	88.8	5.1	50.8	61.1
Real Geometric	March 2018	83.3	84.2	41.0	50.2	91.6	74.7	51.0	92.9	1.0	52.6	71.3
VLS-DL Original	March 2019	62.8	59.7	1.3	29.5	85.4	59.9	35.7	59.5	0	27.3	8.1
VLS-DL Voxel	March 2019	70.0	61.8	16.8	35.7	92.9	69.1	69.0	88.8	1.5	25.2	24.1
Real Geometric	March 2019	80.7	83.6	32.4	43.0	93.3	78.5	53.5	88.5	1.0	46.3	35.7

373 Figure 6 are aggregated on the main categories (“ground” for low vegetation, impervious surface, and soil/gravel;
374 “object” for vehicles, urban furniture, and vertical surface; “building” for roof, facade, and chimney; “non-low vege-
375 tation” for shrub and tree). Both models – the geometric KPConv model trained on real data and the VLS-DL model –
376 offer outstanding performance on point-wise ground classification when there is no need to distinguish between types
377 of ground. Quantitatively, the geometric KPConv model trained on real-world data achieves 92.2% OA and 87.5%
378 MCC in the aggregated semantic segmentation, while when trained on virtual data, it achieves 90.2% OA and 84.5%
379 MCC, respectively.

380 The point-wise classification of building and non-ground vegetation offers promising results for real and virtual
381 models. The many objects in the Hessigheim point clouds (vehicles, urban furniture, and vertical surfaces) are the
382 main problem for both models. An explanation could be that these classes highly benefit from reflectance and RGB
383 information, which was not included in our VLS-DL models. Moreover, some of these classes are also underrepre-
384 sented and have more heterogeneous geometries than others. With 29% of the points of the class “object” correctly
385 classified with the VLS-DL model, compared to 44% with the geometric KPConv model (trained on real data), the re-
386 sults indicate a suboptimal 3D representation of objects (especially vehicles and urban furniture). For urban contexts,
387 the VLS scene model can be significantly improved to fix overly irregular surfaces, missing triangles, and non-smooth
388 orientation changes on some surfaces.

389 A top view of the classified validation point clouds is shown in Figure 7. Visual inspection reveals some coarse
390 grain issues (e.g., the problematic roof at the top), which are similar between real and virtual models. However, the
391 misclassification of small urban objects is a bigger problem for the VLS-DL model (Figure 7a). In a post-processing
392 evaluation, all models perform well when grouping the semantic classes into aggregated categories (Figure 7b). The

393 conclusions from the visual inspection agree with those from the confusion matrices.

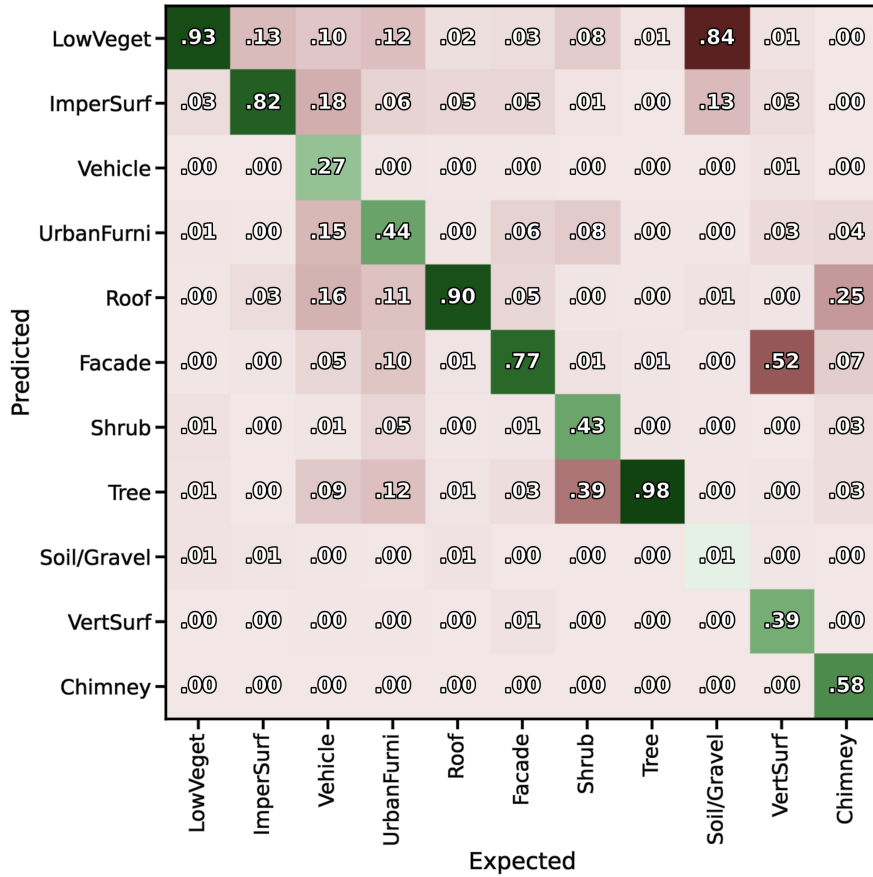


Figure 4: Confusion matrix normalized by expected class for the geometric KPConv model trained on real point clouds from the Hessigheim dataset.

394 4.3. Leaf-wood results

395 Table 7 shows that the results of our FVLS-DL and VLS-DL models are quantitatively within the state-of-the-art
 396 (SOTA) interval for leaf-wood segmentation. The FVLS-DL model is 3% lower in OA than the top SOTA model (Han
 397 and Sánchez-Azofeifa, 2022) whether considering isolated or near trees, while the VLS-DL model is only 2% below
 398 the SOTA considering the near trees experiments. Thus, the performance of both virtual models is near the state-of-
 399 the-art when properly tuned.

400 A general visual impression of point-wise classification on near trees is given in Figure 8 together with the corre-
 401 sponding confusion matrices. All the models give a good approximation of the label reference. The model trained with
 402 reflectance gives the best results and shows the least confusion. However, the differences are small. More concretely,
 403 the reflectance-based model correctly classifies 3% more wood points than the virtual model and just 1% more leaf
 404 points. The real geometric KPConv and the VLS-DL model differ when studying their confusion. More concretely,

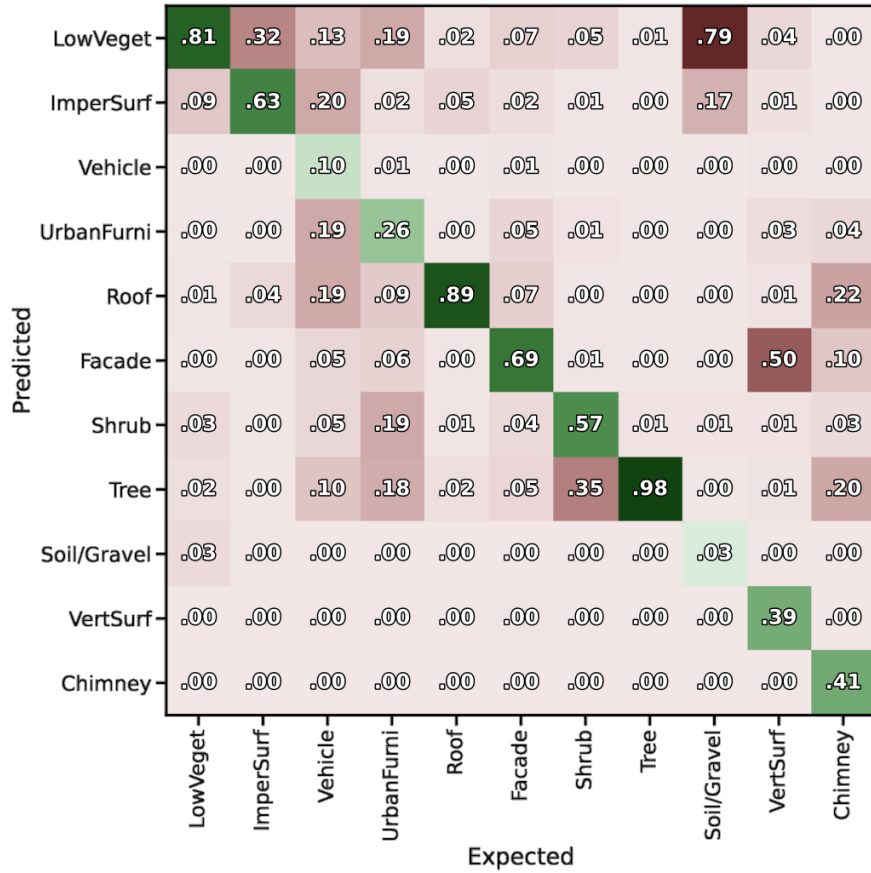


Figure 5: Confusion matrix normalized by expected class for the VLS-DL model applied to the Hessigheim dataset.

405 the geometric KPConv misclassifies more wood points than the VLS-DL model, but the latter misclassifies more leaf
 406 points.

407 Finally, Table 8 represents the quantitative assessment of the FVLS-DL, VLS-DL, and real (geometric only)
 408 models on different datasets. In addition to the point clouds created from Weiser et al. (2023) (results reported in
 409 Tables 4 and 7), the classification performance of the models (Real, VLS-DL and FVLS-DL) was assessed with point
 410 clouds from Wang et al. (2021), for both the isolated and the near trees case, and for point clouds used in Xi et al.
 411 (2020) (Hopkinson, 2020) for just the near trees case (Appendix B). The results reveal that all models generalize
 412 well when tested on different datasets. More specifically, the FVLS-DL model generalizes as well as the real model
 413 to isolated trees with around 93% OA for Weiser and 95% OA for Wang, while the VLS-DL model generalizes to
 414 near trees with just 1% less OA than the real model for Weiser and with a negligible difference of 0.4% OA for Wang.
 415 Concerning the Hopkinson point cloud, the virtual models have around 4% higher OA than the real model. This result
 416 can be explained by the fact that the real model learns more fine-grain details than the virtual ones, and these details
 417 are not present in the Hopkinson point cloud, which is less dense and has some gaps in the wood areas compared to
 418 the others. These results suggest that using VLS to generate targeted training data can lead to better classifications by

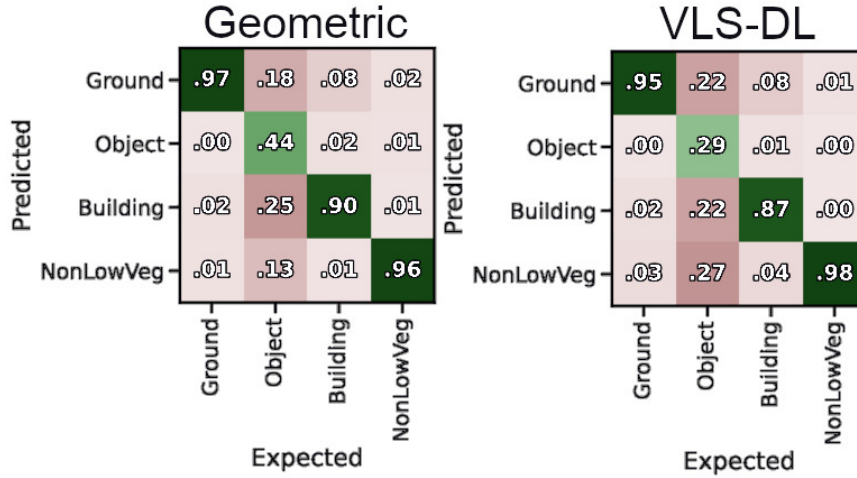


Figure 6: Confusion matrices normalized by expected class with aggregated categories for the geometric KPConv and VLS-DL models on the Hessigheim dataset.

419 providing training point clouds that mimic the particular characteristics of the target dataset.

420 4.4. Mesh sampling, VLS, and real-world point cloud comparison

421 To determine the realism of the physically-based laser scanning simulations, we investigate the difference in
 422 geometric features between the real leaf-wood point clouds, VLS point clouds of the Wytham Woods scene, and point
 423 clouds generated by randomly sampling points on the Wytham Woods mesh. Figure 9 summarizes the main findings
 424 using 2D histograms to show the density of feature values for different heights above ground.

425 First, looking at Figure 9 a), c), and e), note that the distribution shown in the two-dimensional histograms char-
 426 acterizing the training point clouds is significantly different when comparing real or virtual point clouds with mesh
 427 sampling. Visually, the distribution of planarity and linearity is more dispersed for mesh sampling, while it has some
 428 relatively high point concentrations for virtual and real point clouds. While the differences between the real and
 429 virtual training datasets can be explained by the fact that they represent different scenes (mixed forests in Baden-
 430 Württemberg, Germany, and the Wytham Woods research forest in Oxfordshire, United Kingdom, respectively), the
 431 VLS and mesh sampling cases come from the same scene. Furthermore, the white line representing a linear estimator
 432 fitting the feature as a function of height (z coordinate) has very similar slopes and values for virtual and real point
 433 clouds, while it is notably different for the points generated by mesh sampling.

434 Second, the misclassification of geometric KPConv models is shown with respect to the geometric features in the
 435 2D histograms of incorrectly labeled points in Figure 9 b), d), and f). The distributions for virtual and real point
 436 clouds are similar, especially for linearity and planarity. The distributions of the mesh sampling case have more
 437 obvious misclassification concentrations. The conclusions also hold for the linear least-squares fit. These findings
 438 match the quantitative evaluation of the deep learning models shown in Table 7. In terms of performance, the Mesh-
 439 DL model is 42% lower in OA than the VLS-DL model. Moreover, the Mesh-DL model is 36% worse at classifying

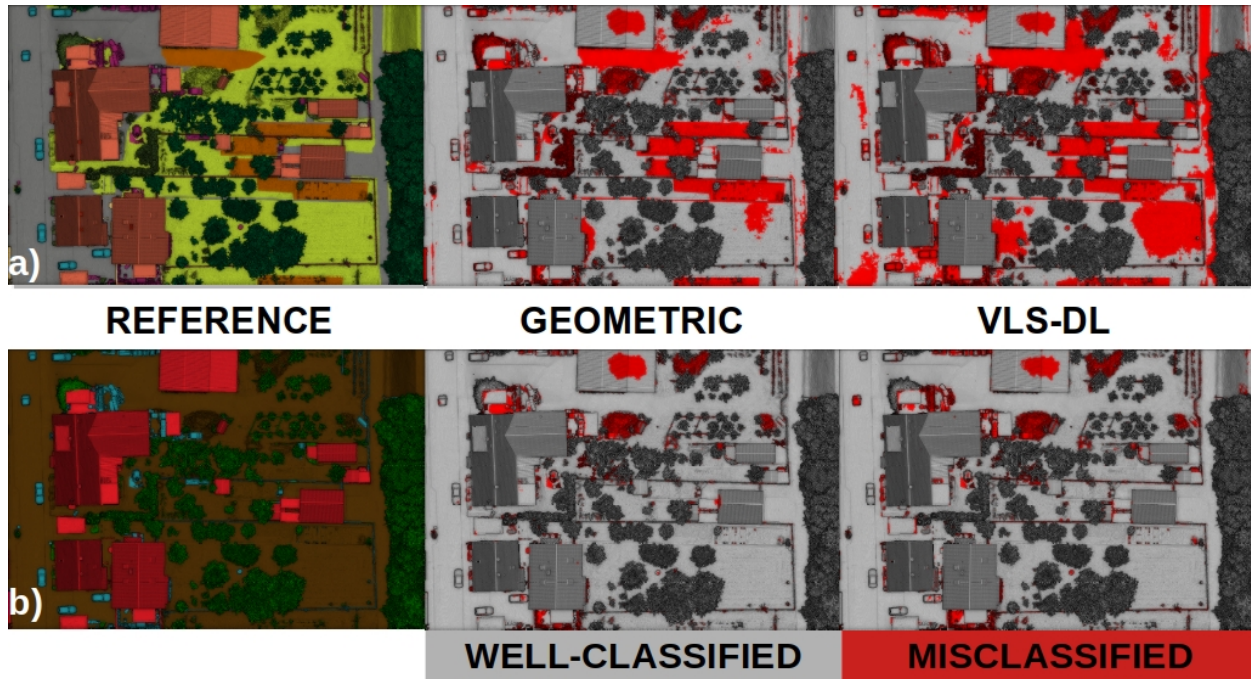


Figure 7: Top view of the reference labels and classification confusion on the validation point cloud. The top row (a) shows the original eleven classes and the confusion from the Hessigheim3D benchmark (Kölle et al., 2021). The bottom row (b) represents our reduced classes: ground, building, vegetation, and object. The gray color represents successfully classified points, while the red represents misclassified points.

440 leaf points than the VLS-DL model, while it is 42% worse at classifying wood points, when measured in terms of F1
 441 score.

442 5. Discussion

443 The results shown in this paper prove that VLS can be used to train DL models without the need for real labeled
 444 reference data. These VLS-based models then generalize to real point clouds. Thus, VLS-DL can reduce the time and
 445 cost associated with industrial and research projects involving machine learning-based classification of point clouds.
 446 The degree to which costs can be reduced depends on the complexity of the 3D scene modeling task. Simple scenes
 447 will significantly reduce time and cost, while complex scenes involving many object types will yield a less significant
 448 reduction due to the more sophisticated 3D modeling required.

449 The VLS-DL model has been tested for the two broader domains in the point cloud processing community: ur-
 450 ban and natural contexts. Each study case requires identifying and improving the key components related to these
 451 categories.

452 5.1. VLS-DL applied to urban contexts

453 From the results of the urban experiments, we understand that the 3D input scene is a critical component for VLS
 454 simulations and that it is affecting the specific classification task. Scene representation problems, such as oversimpli-

Table 7: Comparison between VLS-DL and selected machine learning models from the literature using distinct approaches for the leaf-wood separation problem. The FVLS-DL model is the VLS-DL model trained on fully synthetic trees. The overall accuracy is the aggregated evaluation metric, and the F1 score for leaf and wood is the per-class evaluation metric. The different metrics come from the different datasets used in the corresponding publications. We evaluated our models on the real datasets built from a subset of the Weiser et al. (2023) dataset (Appendix B). The Mesh-DL model is used as a baseline solution to quantify to which extent VLS improves the results of a deep learning model compared to feeding the points from the scene’s meshes directly to the neural network.

Authors	Input	Model	OA	F1 (leaf)	F1 (wood)
Krishna Moorthy et al. (2020)	Multiscale geometric features	Random Forest	94 %	97 %	81 %
		XGBoost	94 %	97 %	81 %
		LightGBM	94 %	96 %	80 %
Vicari et al. (2019)	Geometric features	Unsupervised	89 %	92 %	73 %
Han and Sánchez-Azofeifa (2022)	Geometric features (deep learning)	FCN	92 %	92 %	92 %
		LSTM-FCN	96 %	96 %	96 %
		ResNet	96 %	96 %	96 %
Ours (validated on isolated trees)	FVLS point cloud	FVLS-DL	93 %	96 %	84 %
	VLS point cloud	VLS-DL	87 %	91 %	74 %
Ours (validated on near trees)	FVLS point cloud	FVLS-DL	93 %	96 %	80 %
	VLS point cloud	VLS-DL	94 %	96 %	81 %
	Points from mesh	Mesh-DL	52 %	60 %	39 %

455 fication, lead to lower performance as the realism of the virtual point clouds is reduced. From the results in Table 3,
456 we can see that a voxelized representation of vegetation reduced the OA gap between real and virtual training data by
457 8% compared to using the original mesh-based scene model for VLS. Further improvements are expected to close this
458 gap even more.

459 First, we propose improving VLS with more accurate surface roughness simulation to improve differentiation
460 between natural (e.g., low vegetation) and artificial (e.g., impervious surface) ground. Second, we propose two im-
461 provements for urban object differentiation: 1) the simulation of more scene parts with under-represented objects (e.g.,
462 applying VLS many times with different scene rotations and slight scale changes), and 2) a more accurate representa-
463 tion of vehicles and urban furniture such as fences and streetlights. Lack of detail problems were also mentioned by
464 Wu et al. (2018) when using the default GTA-V physics, leading to simplified representations where pedestrians were
465 treated as cylinders.

466 Furthermore, some problems must be addressed from the DL side (e.g., using different neighborhood definitions).
467 For example, differentiating building facades and vertical surfaces is more related to global context than local neigh-
468 borhood analysis since both are planar surfaces with similar orientation.

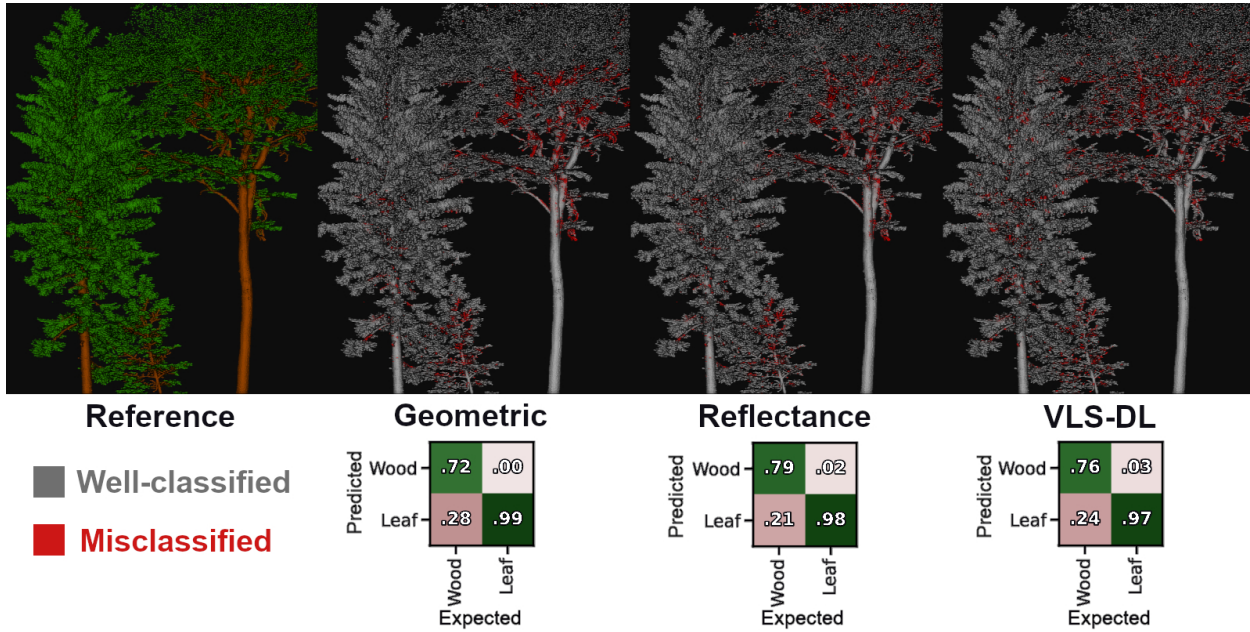


Figure 8: Visualization of leaf-wood segmentation results on real-world tree point clouds (near trees) for the manual labeling (reference), the geometric KPConv model, the reflectance KPConv model, and the VLS-DL model. Points labeled as leaves are colored green, and points labeled as wood are colored brown. The gray points represent successful classifications, while the red ones are misclassifications. The given confusion matrices are normalized by expected class.

469 5.2. VLS-DL applied to leaf-wood segmentation

470 The FVLS-DL and VLS-DL models achieve near state-of-the art results for the leaf-wood case (Table 7) and
 471 achieve satisfactory virtual-to-real generalization on point clouds from different datasets (Table 8). It is expected that
 472 training with VLS data from trees of many different growth forms, leaf shapes and sizes will help to improve the
 473 results. Thus, creating large and diverse training datasets is an advantage of VLS over real data, for which massive
 474 datasets are often unavailable due to the high effort of point cloud acquisition and annotation. Taking advantage of
 475 fully virtual data (FVLS-DL) improved the leaf-wood segmentation of isolated trees by 6.2% OA compared to scene
 476 meshes derived from real point clouds (VLS-DL), as shown in Table 4. This may be due to the higher diversity of the
 477 trees in the FVLS scene, which also includes conifers, compared to the VLS scene, which has only deciduous trees
 478 (mostly sycamore maple, and some ashes and oaks). Furthermore, some applications lack even small labeled datasets
 479 due to the complexity of manually annotating real point clouds. In these cases, VLS is a cost-effective approach to
 480 obtaining labeled training data for deep learning models.

481 5.3. VLS-DL versus mesh sampling

482 The distribution analysis of geometric features (Figure 9) represents an empirical validation of the theoretical
 483 VLS-DL model, as VLS provides a better representation space for feature extraction than sampling points on meshes.
 484 More formally, we show that the interaction of the parametric model described in Section 3.1, the feasible regions

Table 8: Evaluation metrics for the generalization experiments with isolated and near trees, respectively. The real model was trained on real labeled point clouds from the dataset of Weiser et al. (2022), also used for our other experiments. The VLS-DL and FVLS-DL models were trained on simulated point clouds. The VLS-DL models used meshes derived from real data for simulation, while the FVLS-DL model used fully synthetic trees. The validation point clouds are taken from Weiser et al. (2021), from Hopkinson (2020), and from Wang et al. (2021) and are named by the first authors of the data publications.

Validation	Real		VLS-DL			FVLS-DL			
	OA (%)		F1 (%)		OA (%)		F1 (%)		
	Leaf	Wood	Leaf	Wood	Leaf	Wood			
Isolated Weiser	93.5	95.9	85.2	87.0	91.3	74.1	93.2	95.6	84.4
Isolated Wang	95.2	96.5	92.5	87.1	89.8	82.5	95.4	96.5	93.0
Near Weiser	94.7	96.9	83.1	93.7	96.2	81.3	92.6	95.5	79.7
Near Wang	94.7	96.4	90.2	95.1	96.6	91.3	93.8	88.7	96.4
Near Hopkinson	90.1	81.6	93.3	94.5	96.3	88.7	94.5	95.6	89.2

described in Equation 1, and the corresponding physical and convenience constraints leading to the set of points P described in Equation 2 give rise to models that generalize better to real data than those trained using points randomly sampled from the 3D meshes. This clearly underlines the importance of laser scanning simulation and the creation of realistic geographic point clouds.

5.4. VLS-DL hyperparameter tuning

Models trained solely with geometric data have easy-to-understand and easy-to-tune hyperparameters, as illustrated in the aggregated model comparisons of Figure 3. Optimizing the receptive field can be addressed with a simple linear search governed by the cell size of the smallest grid subsampling, yet leading to a significant improvement of the model. The validity of this method holds for both urban and tree point clouds. Moreover, neighborhood topology can be altered to cover a wider area when a more global context is required. This is why de Gélis et al. (2023) used a cylinder-like neighborhood to improve their Siamese KPCConv model. These straightforward modifications have a drastic impact on the performance of the DL model.

Recall that the input matrix \mathbf{P} from Equation 3 can be expressed as a function of continuous variables governing the virtual data. Some variables might be the components of the vector θ defining the simulation constraints in Equation 2. Others might be the variables governing the parametric ray generation model or transformations and constraints on the feasible regions defining the scene. Consequently, it must be possible to optimize the VLS model parameters too.

We argue that the feature extraction operator, especially when considering classes separable from geometric information, can link the VLS and the DL models. Therefore, fitting the simulator to maximize the class separability of the feature extraction operator inside the VLS model should improve the performance of a DL model using the same operator. To do this, first, a realistic simulation is needed as a baseline. Then, the realistic simulation could be

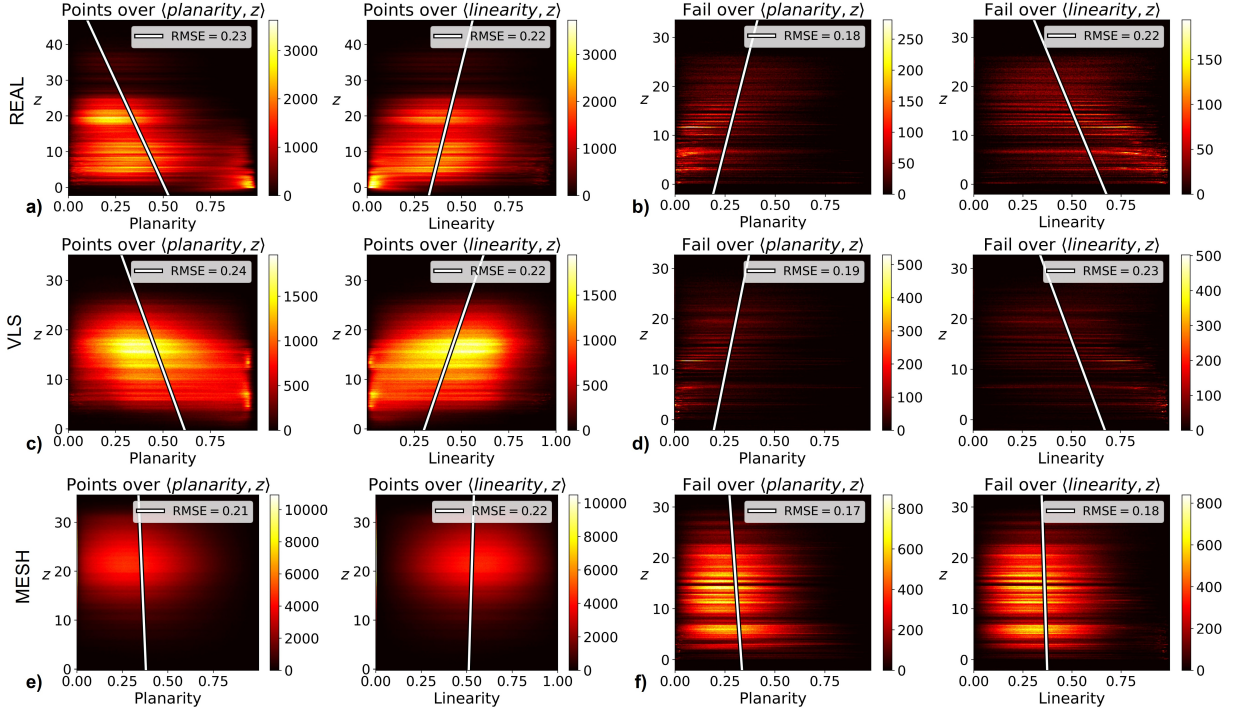


Figure 9: Distribution of geometric features along the z axis for mesh sampling, VLS, and real point clouds. The top row shows a) the feature distribution in the real point cloud and b) the feature distribution of misclassified real points for a model trained on real data. The middle row shows c) the feature distribution in the VLS point cloud and d) the feature distribution of misclassified real points for a model trained on VLS data. The bottom row shows e) the feature distribution in the mesh sampling point cloud and f) the feature distribution of misclassified real points for a model trained from the mesh sampling point cloud. The white line is the best linear fit of the feature as a function of the height (z).

505 optimized to maximize the adequacy of the VLS point cloud as training data for a particular task. Loosing too much
 506 realism will break the relationship between virtual training data and real validation data, so the optimization must be
 507 constrained to stick to slight transformations.

508 It is possible to quantify and visualize the differences between virtual and real point clouds using continuous
 509 metrics derived from the geometry of a neighborhood, as shown in Figure 9. These measurements are similar to the
 510 classification error distribution. Thus, tuning the VLS model to improve the class-separability of the extracted features
 511 while keeping them realistic should improve the DL model’s performance.

512 5.5. VLS-DL cost and automation

513 If an appropriate model of a labeled scene is available, VLS generates perfectly labeled training data for DL with-
 514 out costly equipment other than a computer. The performance of a classifier trained with VLS data can be improved
 515 in different ways. On the one hand, improving the ray-generation model can be done by looking at manufacturer spec-
 516 ifications, often offered as open-access documents at no cost. Also, some open-access simulators like HELIOS++
 517 provide ways to automatically derive an accurate parametric platform model through interpolation from raw trajec-

518 tory files that can be simulated or reused at no extra cost. On the other hand, scene modeling is potentially the most
519 expensive cost for the VLS-DL model, requiring more time and often human involvement. Nevertheless, it is also
520 crucial to simulate a proper training dataset, and poor scenes lead to poor point clouds, which have little to no ben-
521 efit in training DL models. More particularly, when complex scene modeling relies on hand-crafted meshes, buying
522 high-quality meshes or commercial software or hiring a 3D modeling professional will significantly increase the cost.
523 However, this increased cost can be amortized for those cases where the same scene can be used to generate different
524 point clouds.

525 Fortunately, there are several ways in which the scene modeling problem can be tackled. Sometimes, high-quality
526 meshes can be automatically derived from real data. For example, using high-resolution and accurate LiDAR or pho-
527 togrammetry sensors to obtain reliable input data for meshing algorithms. Another alternative is to use procedurally
528 generated meshes. The first benefit of these approaches is that they keep the cost of VLS-DL low. More importantly,
529 they also open up the gate to fully automatic workflows. Specifically, when the scene representing the object for study
530 can be procedurally generated, the whole VLS-DL model can be fully automated because all the other parts of the
531 workflow are already available as interaction-free tools. In general, we believe that the benefits of VLS-DL outweigh
532 the challenges identified.

533 **6. Future challenges**

534 *6.1. VLS-DL for regression*

535 Machine learning problems can be divided into two broad categories: classification and regression. The VLS-DL
536 model has proven good enough to solve classification problems on real point clouds. Now, regression problems are a
537 relevant next milestone. Exploring regression on point clouds will allow us to study how the VLS-DL model performs
538 when it must compute continuous values on a point cloud instead of assigning a discrete class value for each point.
539 For instance, the output of the leaf-wood segmentation model can be used to train a regression model on the wood
540 points to compute biomass estimations. Also, the leaf points can be used to estimate the leaf area index, an important
541 ecological parameter that can be used to estimate the energy flow in the leaves and the expected productivity of a tree.

542 *6.2. Tuning Virtual Laser Scanning*

543 In this work, we showed that the VLS-DL model could be seen as a combined model such that both the simulator
544 and the neural network can be tuned to improve the overall model performance. We also showed that changes in VLS
545 imply changes in DL performance. These changes were characterized using continuous geometric features and linear
546 fitting. Future efforts to improve the VLS-DL model should aim at integrating the feature extractor operator into the
547 simulator to perform fine-grain tuning to maximize the class separability of the features or to minimize the difference
548 to a reference point cloud. If the previously described integration is achieved, starting the optimization algorithm
549 directly in the VLS model should work as long as 1) the VLS optimization starts from a realistic simulation and 2) the
550 VLS optimization is constrained to avoid drastic transformations that deviate too far from the realistic baseline.

551 Furthermore, when procedurally generated 3D scenes are realistic enough, the VLS tuning can be fully automated.
552 Exploring procedural generation algorithms for 3D scenes is relevant to future research towards fully automatic VLS-
553 DL. In this case, hyperparameter tuning could be fully automated through random and grid search strategies, genetic
554 algorithms, or particle swarm optimization, as usually done in automated machine learning (Das and Cakmak, 2018).
555 In this work, we explored the combination of VLS-DL with procedurally generated trees with successful results.
556 Other works have explored artificial intelligence models like Generative Adversarial Networks (GANs) for point
557 cloud processing in the context of robotics and autonomous driving (Goodfellow et al., 2014; Caccia et al., 2019;
558 Triess et al., 2022).

559 *6.3. Dynamic Virtual Laser Scanning*

560 Until now, VLS has typically been computed assuming a static scene. However, laser scanning is often used in
561 real-world contexts with changing conditions (e.g., moving vehicles and pedestrians or moving trees with leaf flutter
562 and branch buffeting due to wind). The VLS-DL model should also be made compatible with dynamic VLS, i.e.,
563 with simulations in which the scene changes over time. By extending VLS to support dynamic scenes, the VLS-DL
564 model can be trained on point distributions explained by motion, including certain scanning artifacts and motion-
565 caused occlusions. For example, the open-source software HELIOS++ has recently included support for dynamic
566 VLS, which opens up the gate for future research in this direction.

567 **7. Conclusions**

568 In this paper, we showed that deep learning models trained solely with virtual laser scanning (VLS) data can be
569 used to semantically segment real point clouds with high accuracy. Training with real data leads to an overall accuracy
570 (OA) 1% higher than training with virtual data in our leaf-wood experiments, and 7% to 8.3% higher in our urban
571 experiments. We almost closed the gap between VLS and reality for the leaf-wood segmentation problem, achieving
572 near state-of-the-art results with full VLS-based training. For semantic segmentation in urban contexts, we started to
573 close the gap between VLS and reality, reducing the difference in OA from 16.3% and 17.5% to 8.3% and 7% for the
574 2018 and 2019 point clouds, respectively, by improving the 3D scene with voxel-based vegetation modeling. Also, we
575 show that fully automatic scene generation and model training is possible with our FVLS-DL model, which is based
576 on a fully computer generated virtual scene.

577 The theoretical description of VLS-DL and the empirical validation from our experiments suggest that a deeper
578 integration of both models is possible. Moreover, while our results are satisfactory, improving them requires human-
579 based manual work to tune the hyperparameters and design realistic 3D scenes. While this work is not so laborious
580 and prone to errors as manual labeling, better integration of VLS-DL could alleviate this burden by automatizing
581 fine-grain tuning and bringing optimization from DL to VLS. Furthermore, if procedurally generated scenes can be
582 computed with sufficient realism, the entire workflow can be optimized automatically.

583 We consider there is enough evidence to claim that VLS is a convenient solution for training a wide variety of point
584 cloud classifiers based on supervised training. Furthermore, the time and cost-saving potential of VLS-DL makes it a
585 viable option for point cloud research and industrial applications. Typical problems, such as insufficient or imbalanced
586 data, can be addressed using VLS-generated data. Thus, taking advantage of virtual laser scanning can revolutionize
587 deep learning applied to point clouds.

588 **8. Declaration of competing interests**

589 The authors declare that they have no competing interests influencing this paper.

590 **9. Acknowledgement**

591 This research was funded by the Deutsche Forschungsgemeinschaft (DFG), German Research Foundation, by
592 the projects SYSSIFOSS (Grant Number: 411263134) and VirtualLearn3D (Grant Number: 496418931). It was
593 furthermore supported by the BMBF (Federal Ministry for Education and Research, Germany) in the frame of the
594 AImon5.0 project (funding code: 02WDG1696).

595 This work has also received financial support from the Consellería de Cultura, Educación e Ordenación Universi-
596 taria (accreditation ED431C 2022/16 and accreditation ED431G-2019/04) and the European Regional Development
597 Fund (ERDF), which acknowledges the CiTIUS-Research Center in Intelligent Technologies of the University of
598 Santiago de Compostela as a Research Center of the Galician University System, and the Ministry of Economy and
599 Competitiveness, Government of Spain (Grant Number PID2019-104834GB-I00 and PID2022-141623NB-I00).

600 The many deep learning experiments computed on the FinisTerra-III supercomputer were possible thanks to the
601 CESGA (Galician supercomputing center). Diverse experiments were also possible thanks to the data curators of the
602 Hessigheim and Wytham Woods datasets and the manually labeled leaf-wood datasets.

603 **Appendix A. Virtual Scene Generation and Virtual Laser Scanning**

604 *Appendix A.1. Urban Scene Classification*

605 *Creating the Virtual Scenes*

606 The Hessigheim 3D (H3D) benchmark dataset (Kölle et al., 2021) is already split into training and validation. We
607 used the training subsets of the meshes and the point clouds to create two versions of the 3D scene for our laser scan-
608 ning simulations. For both versions, a modified material library (.MTL file) with an added `helios_classification`
609 value was used. An example for one material is shown below:

```
610 newmtl Low Vegetation  
611 Ka 0.698039 0.796078 0.184314  
612 Kd 0.698039 0.796078 0.184314
```

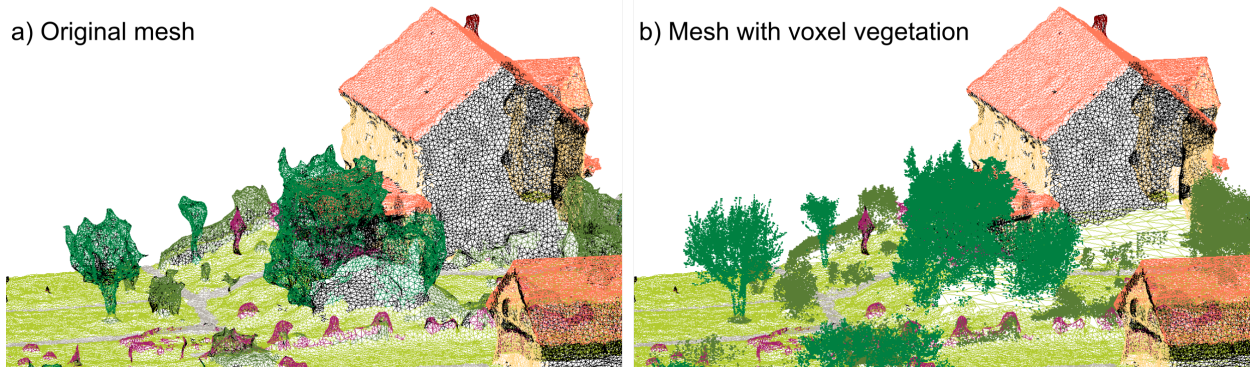


Figure A.10: Comparison of a) the original Hessigheim 3D mesh and b) the modified Hessigheim 3D mesh with voxelized vegetation. Colored by classification.

```

613 Ks 0.698039 0.796078 0.184314
614 illum 2
615 Ns 136.430000
616 helios_classification 0

```

617 In this way, the simulated returns are automatically assigned the `helios_classification` value of the material
618 of the surface which they hit.

619 Version 1 of our H3D virtual scene uses the original mesh tiles from the H3D training dataset. Version 2 of
620 our H3D virtual scene uses a modified scene representation, where vegetation (classes "shrub" and "tree", as well
621 as all faces labeled as "unlabeled" in the close vicinity of vegetation classes) have been removed from the mesh
622 and instead modeled using voxels. For this, vegetation points were filtered from the H3D training point clouds and
623 transformed into voxel models with $5\text{ cm} \times 5\text{ cm} \times 5\text{ cm}$ voxels using the HELIOS++ xyzloader³. After removing
624 faces classified as vegetation from the mesh, the 3D model contains holes (below the now semi-transparent voxel
625 vegetation representations). To fill these holes, we added a digital terrain model (DTM) to the scene, which we
626 generated from the ground points of the H3D point cloud (classes low vegetation, impervious surface, soil/gravel).
627 This DTM was shifted downwards by 0.2 m to ensure that it does not cover or intersect with other parts of the scene
628 and assigned the material (i.e., classification) "low vegetation". Figure A.10 compares the two versions.

629 *Virtual Laser Scanning Configuration*

630 A trajectory of one of the Hessigheim ULS campaigns (columns: X, Y, Z, roll, pitch, yaw) was provided by
631 colleagues at the Institute for Photogrammetry and Geoinformatics at the University of Stuttgart. It consists of three
632 separate flights. The trajectory points were converted into a line feature and then simplified using the Douglas Peucker
633 algorithm. The waypoints of the simplified lines were then used in the survey XML file for the X-Y "leg" positions.

³<https://github.com/3dgeo-heidelberg/helios/wiki/Scene#xyz-point-cloud-loader> (Accessed on 2 October 2023)

634 The heights of the waypoints were obtained from the original trajectory point file. For the 2019 surveys for training,
 635 some waypoints were moved further out along the Y-direction to ensure that the entire mesh is scanned.
 636 Acquisition settings were selected to match the real data acquisition and are shown in Table A.9.

Table A.9: ULS scan settings used for the Hessigheim HELIOS++ simulations.

Setting	Value
Scanner	<i>RIEGL VUX-1LR</i>
Scan angle	$\pm 35^\circ$ off nadir
Pulse frequency	820 kHz
Scan frequency	133 Hz
UAV speed	8 m/s

637 *Resulting VLS Point Clouds for Model Training*

638 Figure A.11 shows the real and the two different VLS point clouds. The number of intermediate returns is several
 639 hundred times lower when using the original mesh in the simulations than when using the modified 3D scene with
 640 voxel vegetation. Unlike the mesh, the simulated laser beam can penetrate the voxelized canopies and thus generate
 641 multiple returns, making the simulation more realistic. This can also be seen visually in Figure A.11. The number
 642 of intermediate returns in the VLS point cloud with voxel vegetation is in the same order of magnitude as in the real
 643 point cloud.

644 Pulse density is lower in the VLS point clouds than in the real point clouds in both 2018 (VLS original: 720 pts/m²,
 645 VLS voxel: 740 pts/m², real: 1050 pts/m²) and 2019 epochs (VLS original: 820 pts/m², VLS voxel: 870 pts/m²,
 646 real: 910 pts/m²). This may be due to different reasons: 1) While the publication states 8 m/s as the speed of the UAV,
 647 the UAV does not move with constant speed in reality and might have been slower due to wind or due to the necessary
 648 deceleration and acceleration in the corners when turning. Due to a lack of the GPS Time attribute in the real point
 649 clouds, or an identifier for the flight strip, in-depth investigations of these differences were not feasible. 2) The mesh
 650 contains unlabeled faces. As we are not training on the "unlabeled" class, we removed it from the simulated point
 651 cloud, which lowers the number of points.

652 *Appendix A.2. Leaf-wood Classification*

653 *Creating the Virtual Scenes*

654 With our experiments on leaf-wood classification using VLS training data, we cover two central ways of generating
 655 virtual scenes: a) procedural 3D modelling with no real data at all, and b) the reconstruction of a real scene from 3D
 656 measurements such as photogrammetric and/or laser scanning point clouds.

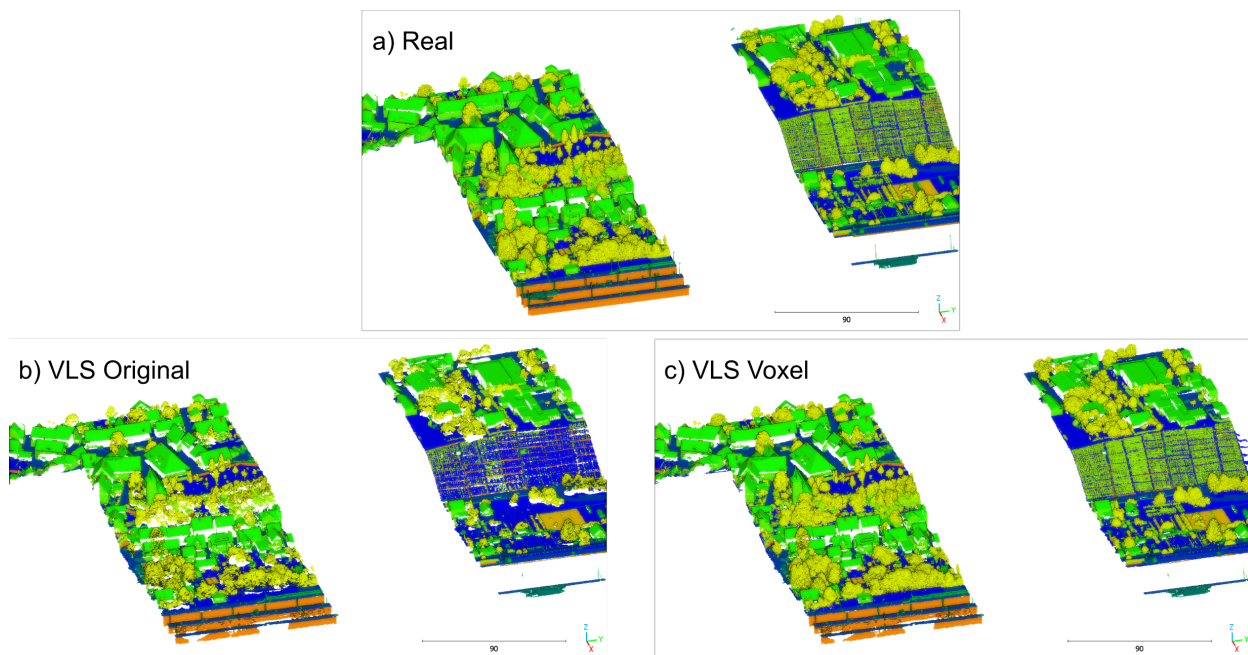


Figure A.11: Images of a) the training subset of real Hessigheim 3D point cloud, b) the simulated point cloud using the original Hessigheim3D mesh, and c) the simulated point cloud using the modified Hessigheim 3D scene with vegetation represented by voxels (all March 2019 epoch). Colored by classification.

657 The fully synthetic scenes were assembled using procedurally generated 3D tree models of trees. These were
 658 generated using the algorithm of Weber and Penn (1995), implemented in the add-on "Sapling Tree Gen"⁴ in the
 659 open-source 3D modelling software Blender (Blender Online Community, 2023). 10 different trees were created by
 660 modifying the various parameters. Three were conifers with needles and seven were broadleaf trees with different leaf
 661 shapes. For each tree, two more trees were created by changing the random seed, resulting in a total of 30 trees. The
 662 trees were arranged in a small forest stand, with their crowns clearly overlapping (Figure A.12a).

663 For the second option, scenes reconstructed from real data, we used the Wytham Woods 3D model, which is
 664 openly available⁵ (Calders et al., 2018; Liu et al., 2022). We used the positions and tree mesh models (.OBJ files) in
 665 the `DART_models/3D-explicit` model folder in the branch `add_dart`.

666 It is important to note that due to the conversion of the cylindrical quantitative structure models (QSMs) to trian-
 667 gular meshes, the trunks and branches of the tree models are angular rather than round. Leaves are modeled as flat
 668 elongated hexagons.

669 We have modified the material library (.MTL) file to add the `helios_classification_0` to the material "Trunk-
 670 AndBranches", and 1 to the material "Leaves". The trees were split spatially into training and test by manually

⁴https://docs.blender.org/manual/en/latest/addons/add_curve/sapling.html (Accessed on 11 August 2023)

⁵https://bitbucket.org/tree_research/wytham_woods_3d_model/src/add_dart/DART_models/ (Accessed on 19 October 2022)

Table A.10: TLS scan settings used for the HELIOS++ simulations for the leaf-wood experiments. For the fully virtual trees (FVLS) and the isolated Wytham Woods trees (VLS isolated), a higher resolution was used than for the full Wytham Woods forest stand (VLS near).

Setting	Value		
Scanner	<i>RIEGL VZ-400</i>		
Vertical field of view	-40° – 60°		
Pulse frequency	300 kHz		
Effective measurement rate	122 kHz		
	FVLS, VLS isolated	VLS near (Wytham Woods forest)	
Horizontal resolution	0.017°	0.04°	
Vertical resolution	0.017°	0.04°	
Vertical point spacing (10 m range)	3 mm	7 mm	
Horizontal point spacing (10 m range)	3 mm	7 mm	

671 extracting a quarter of the area to be used for testing.

672 Besides the full Wytham Woods forest scene (“near trees”), we created six scenes, in which eight trees were
673 randomly drawn from the Wytham Woods dataset (without replacement) and assembled into a common scene with
674 plenty of space between them (Figure A.12c). We call this version “isolated trees” because the crowns of the trees do
675 not overlap and no input neighborhood of one tree contains any points of another tree.

676 *Virtual Laser Scanning Configuration*

677 The acquisition settings for all three leaf-wood experiments are summarized in Table A.10. The synthetic forest
678 stand of fully computer-generated trees was scanned from six scan positions using a virtual terrestrial laser scanner
679 of the model *RIEGL VZ-400*. The scan positions were regularly distributed on a 60 m radius circle around the trees
680 and were oriented toward the forest plot center, scanning a horizontal field of view (FOV) of 90°. The Wytham
681 Woods scene of the full forest stand was virtually scanned from 15 scan positions. These were manually distributed
682 on the boundaries and inside the forest plot. The horizontal FOVs were defined based on the positions, so that a full
683 360° scan is performed for the scan positions within the forest plot and smaller FOVs were used for positions at the
684 boundaries. The simulated training point cloud is shown in Figure A.12b. Simulations were carried out the same way
685 for the smaller validation scene but using only four scan positions. The scenes with isolated Wytham Woods trees
686 were virtually scanned from six positions, evenly spaced on a circle of 35 m radius around the trees. Each scan had a
687 horizontal FOV of 90°.

688 *Resulting VLS Point Clouds*

689 Resulting simulated VLS point clouds for training the VLS-based leaf-wood classifiers are displayed in Fig-
690 ure A.12. We refer to the point clouds of the procedurally modeled trees (Figure A.12a) as “fully virtual laser scanning

691 (FVLS)” point clouds and to the models trained with them as FVLS-DL models.

692 The point clouds of the Wytham Woods tree models (Figure A.12b and c) are referred to as VLS point clouds
693 (near trees and isolated trees, respectively) and the models are referred to as VLS-DL models.

694 **Appendix B. Real point clouds for training and validation**

695 The real urban classification models were trained on the real training point clouds of the Hessigheim 3D bench-
696 mark. All models for urban classification, real, VLS original and VLS voxel, were evaluated using the validation point
697 clouds in the Hessigheim 3D benchmark.

698 For leaf-wood classification, two real models were trained, one on a point cloud of isolated trees and one on a
699 point cloud with near trees (Figure B.13) with eight labeled tree point clouds from Weiser et al. (2023). Each tree was
700 individually normalized by subtracting the ground elevation at the location of the tree trunk and then re-positioned in
701 a common point cloud in a local coordinate system.

702 The isolated trees training point cloud was composed of the tree point clouds with the IDs AcePse_SP02_04,
703 FagSyl_BR01_01, FagSyl_BR05_P8T4, PicAbi_BR02_14, PinSyl_KA10_03, PseMen_BR04_02, QuePet_BR01_01,
704 and QueRub_KA09_T053 and the point clouds were spread out with a lot of space in between each tree.

705 The near trees training point cloud was composed of the tree point clouds with the IDs AcePse_SP02_04, FagSyl_BR01_01,
706 PicAbi_BR02_14, PinSyl_KA09_T048, PinSyl_KA10_03, PseMen_BR04_02, QuePet_BR01_01, and QueRub_KA11_09.
707 They were so closely spaced, that their crowns may touch or overlap (Figure B.13a).

708 The main validation datasets for this study were generated from the remaining trees of the labeled tree point cloud
709 dataset (Weiser et al. (2023)), respectively. For the isolated trees, these were PicAbi_BR08_01, PinSyl_KA09_T048,
710 QueRub_KA11_09, for the near trees with ground, these were FagSyl_BR05_P8T4, PicAbi_BR08_01, QueRub_KA09_T053
711 (Figure B.13b).

712 In addition, we used subsets of the datasets by Wang et al. (2021) and Hopkinson (2020) as real validation point
713 clouds (Table 8). The ”Isolated Wang” dataset was composed of the point clouds with the IDs 2, 11, 18, 68, 96, 97,
714 and 102. The ”Near Wang” dataset was composed of the point clouds with the IDs 4, 5, 12, 18, 31, 32, 57, 59, 60, 63,
715 73, 75, 83, 87, 88, 89, 92 93, 95, 96, 100, 101, and 104. Finally, the ”Near Hopkinson” validation dataset consisted of
716 the point clouds named MDD04_012, MDD06_007, MDD07_010, MDD08_006, and MDD09_007.

717 **References**

- 718 Ao, Z., Wu, F., Hu, S., Sun, Y., Su, Y., Guo, Q., Xin, Q., 2022. Automatic segmentation of stem and leaf components and individual maize plants
719 in field terrestrial LiDAR data using convolutional neural networks. *The Crop Journal* 10, 1239–1250. doi:<https://doi.org/10.1016/j.cj.2021.10.010>.
- 720
- 721 Armeni, I., Sener, O., Zamir, A.R., Jiang, H., Brilakis, I., Fischer, M., Savarese, S., 2016. 3D Semantic Parsing of Large-Scale Indoor Spaces,
722 in: 2016 IEEE Conference on Computer Vision and Pattern Recognition (CVPR), pp. 1534–1543. doi:<https://doi.org/10.1109/CVPR.2016.170>.
- 723

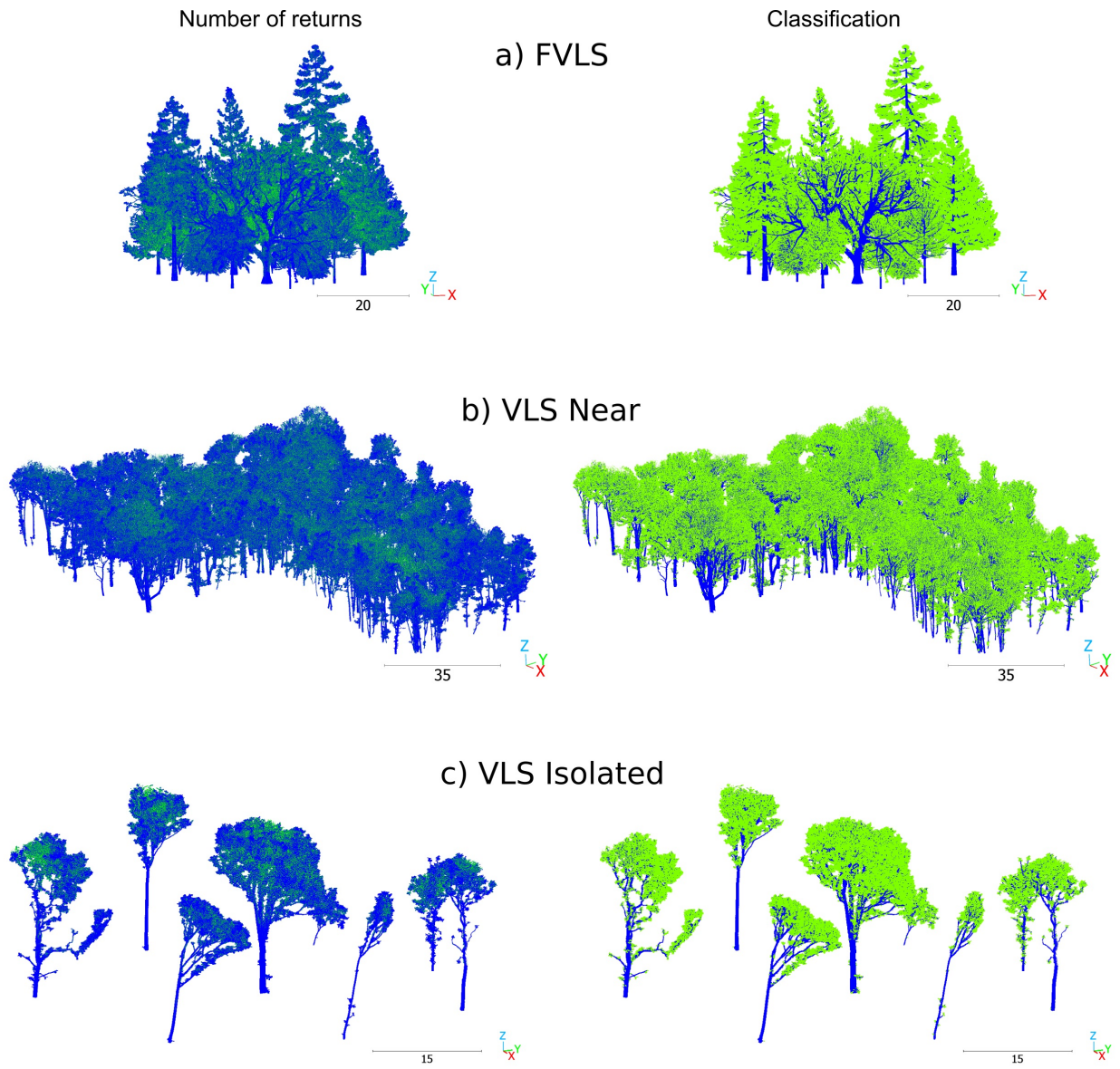


Figure A.12: Simulated point clouds of a) the fully virtual synthetic scenes with procedurally generated tree models, b) the Wytham Woods scene, and c) the isolated Wytham Woods scene. Colored by number of returns (left) and classification (right).

a) Training



b) Validation

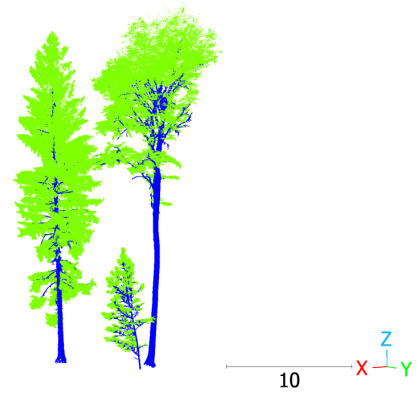


Figure B.13: Real training and validation point clouds for leaf-wood separation with trees from Weiser et al. (2023). Coloured by classification: green=leaf, blue=wood, yellow=ground.

- 724 Blender Online Community, 2023. Blender - a 3D modelling and rendering package. URL: <https://www.blender.org/>.
- 725 Boni Vicari, M., Disney, M., Wilkes, P., Burt, A., Calders, K., 2018a. Leaf and wood classification framework for terrestrial LiDAR point clouds:
726 Field data validation dataset. doi:<https://doi.org/10.5281/zenodo.1324156>.
- 727 Boni Vicari, M., Disney, M., Woodgate, W., 2018b. Leaf and wood classification framework for terrestrial LiDAR point clouds: Simulated data
728 validation dataset. doi:<https://doi.org/10.5281/zenodo.1324158>.
- 729 Boyd, S., Vandenberghe, L., 2004. Convex optimization. Cambridge university press.
- 730 Bryson, M., Wang, F., Allworth, J., 2023. Using Synthetic Tree Data in Deep Learning-Based Tree Segmentation Using LiDAR Point Clouds.
731 Remote Sensing 15. URL: <https://www.mdpi.com/2072-4292/15/9/2380>, doi:<https://doi.org/10.3390/rs15092380>.
- 732 Caccia, L., Hoof, H.v., Courville, A., Pineau, J., 2019. Deep Generative Modeling of LiDAR Data, in: 2019 IEEE/RSJ International Conference
733 on Intelligent Robots and Systems (IROS), pp. 5034–5040. doi:<https://doi.org/10.1109/IR0S40897.2019.8968535>.
- 734 Calders, K., Origo, N., Burt, A., Disney, M., Nightingale, J., Raunonen, P., Åkerblom, M., Malhi, Y., Lewis, P., 2018. Realistic Forest Stand Re-
735 construction from Terrestrial LiDAR for Radiative Transfer Modelling. Remote Sensing 10. doi:<https://doi.org/10.3390/rs10060933>.
- 736 Cohen, J., 1960. A coefficient of agreement for nominal scales. Educational and Psychological Measurement 20, 37–46. doi:<https://doi.org/10.1177/001316446002000104>.
- 737
- 738 Cramer, M., Haala, N., Laupheimer, D., Mandlburger, G., Havel, P., 2018. ULTRA-HIGH PRECISION UAV-BASED LIDAR AND DENSE
739 IMAGE MATCHING. The International Archives of the Photogrammetry, Remote Sensing and Spatial Information Sciences XLII-1, 115–120.
740 doi:<https://doi.org/10.5194/isprs-archives-XLII-1-115-2018>.
- 741 Das, S., Cakmak, U.M., 2018. Hands-On Automated Machine Learning: A Beginner's Guide to Building Automated Machine Learning Systems
742 Using AutoML and Python. Packt Publishing.
- 743 de Gélis, I., Lefèvre, S., Corpetti, T., 2023. Siamese KPConv: 3D multiple change detection from raw point clouds using deep learning. ISPRS
744 Journal of Photogrammetry and Remote Sensing 197, 274–291. doi:<https://doi.org/10.1016/j.isprsjprs.2023.02.001>.
- 745 Dosovitskiy, A., Ros, G., Codevilla, F., Lopez, A., Koltun, V., 2017. CARLA: An open urban driving simulator, in: Proceedings of the 1st Annual
746 Conference on Robot Learning, pp. 1–16.
- 747 Esmoris, A.M., Yermo, M., Weiser, H., Winiwarter, L., Höfle, B., Rivera, F.F., 2022. Virtual LiDAR Simulation as a High Performance Computing
748 Challenge: Toward HPC HELIOS++. IEEE Access 10, 105052–105073. doi:<https://doi.org/10.1109/ACCESS.2022.3211072>.

- 749 Ferrara, R., Virdis, S.G., Ventura, A., Ghisu, T., Duce, P., Pellizzaro, G., 2018. An automated approach for wood-leaf separation from terrestrial
750 LIDAR point clouds using the density based clustering algorithm DBSCAN. *Agricultural and Forest Meteorology* 262, 434–444. doi:<https://doi.org/10.1016/j.agrformet.2018.04.008>.
- 751
- 752 Gao, F., Yan, Y., Lin, H., Shi, R., 2022. PIIE-DSA-Net for 3D Semantic Segmentation of Urban Indoor and Outdoor Datasets. *Remote Sensing* 14.
753 doi:<https://doi.org/10.3390/rs14153583>.
- 754 Gastellu-Etchegorry, J.P., Yin, T., Lauret, N., Grau, E., Rubio, J., Cook, B.D., Morton, D.C., Sun, G., 2016. Simulation of satellite, airborne and
755 terrestrial LiDAR with DART (I): Waveform simulation with quasi-Monte Carlo ray tracing. *Remote Sensing of Environment* 184, 418–435.
756 doi:<https://doi.org/10.1016/j.rse.2016.07.010>.
- 757 Geiger, A., Lenz, P., Urtasun, R., 2012. Are we ready for autonomous driving? The KITTI vision benchmark suite, in: 2012 IEEE Conference on
758 Computer Vision and Pattern Recognition, pp. 3354–3361. doi:<https://doi.org/10.1109/CVPR.2012.6248074>.
- 759 Goodfellow, I., Bengio, Y., Courville, A., 2016. *Deep learning*. The MIT Press.
- 760 Goodfellow, I., Pouget-Abadie, J., Mirza, M., Xu, B., Warde-Farley, D., Ozair, S., Courville, A., Bengio, Y., 2014. Generative
761 Adversarial Nets, in: Ghahramani, Z., Welling, M., Cortes, C., Lawrence, N., Weinberger, K. (Eds.), *Advances in Neural Infor-*
762 *mation Processing Systems*, Curran Associates, Inc. URL: [https://proceedings.neurips.cc/paper_files/paper/2014/file/](https://proceedings.neurips.cc/paper_files/paper/2014/file/5ca3e9b122f61f8f06494c97b1afccf3-Paper.pdf)
763 [5ca3e9b122f61f8f06494c97b1afccf3-Paper.pdf](https://proceedings.neurips.cc/paper_files/paper/2014/file/5ca3e9b122f61f8f06494c97b1afccf3-Paper.pdf).
- 764 Graham, B., 2015. Sparse 3D convolutional neural networks, in: Xie, X., Jones, M.W., Tam, G.K.L. (Eds.), *Proceedings of the British Machine*
765 *Vision Conference 2015, BMVC 2015, Swansea, UK, September 7-10, 2015*, BMVA Press, pp. 150.1–150.9. URL: [https://doi.org/10.](https://doi.org/10.5244/C.29.150)
766 [5244/C.29.150](https://doi.org/10.5244/C.29.150), doi:10.5244/C.29.150.
- 767 Graham, B., Engelcke, M., Maaten, L., 2018. 3D Semantic Segmentation with Submanifold Sparse Convolutional Networks, in: 2018 IEEE/CVF
768 Conference on Computer Vision and Pattern Recognition (CVPR), IEEE Computer Society, Los Alamitos, CA, USA, pp. 9224–9232. URL:
769 <https://doi.ieeecomputersociety.org/10.1109/CVPR.2018.00961>, doi:10.1109/CVPR.2018.00961.
- 770 Griffiths, D., Boehm, J., 2019. A Review on Deep Learning Techniques for 3D Sensed Data Classification. *Remote Sensing* 11. doi:<https://doi.org/10.3390/rs11121499>.
- 771
- 772 Gschwandtner, M., Kwitt, R., Uhl, A., Pree, W., 2011. BlenSor: Blender Sensor Simulation Toolbox, in: Bebis, G., Boyle, R., Parvin, B., Koracin,
773 D., Wang, S., Kyunghnam, K., Benes, B., Moreland, K., Borst, C., DiVerdi, S., Yi-Jen, C., Ming, J. (Eds.), *Advances in Visual Computing*,
774 Springer Berlin Heidelberg, Berlin, Heidelberg, pp. 199–208.
- 775 Guo, Y., Wang, H., Hu, Q., Liu, H., Liu, L., Bennamoun, M., 2021. Deep Learning for 3D Point Clouds: A Survey. *IEEE Transactions on Pattern*
776 *Analysis and Machine Intelligence* 43, 4338–4364. doi:<https://doi.org/10.1109/TPAMI.2020.3005434>.
- 777 Hackel, T., Savinov, N., Ladicky, L., Wegner, J.D., Schindler, K., Pollefeys, M., 2017. SEMANTIC3D.NET: A new large-scale point cloud
778 classification benchmark, in: *ISPRS Annals of the Photogrammetry, Remote Sensing and Spatial Information Sciences*, pp. 91–98.
- 779 Hackel, T., Wegner, J.D., Schindler, K., 2016. FAST SEMANTIC SEGMENTATION OF 3D POINT CLOUDS WITH STRONGLY VARYING
780 DENSITY. *ISPRS Annals of the Photogrammetry, Remote Sensing and Spatial Information Sciences III-3*, 177–184. doi:[https://doi.org/](https://doi.org/10.5194/isprs-annals-III-3-177-2016)
781 [10.5194/isprs-annals-III-3-177-2016](https://doi.org/10.5194/isprs-annals-III-3-177-2016).
- 782 Han, T., Sánchez-Azofeifa, G.A., 2022. A Deep Learning Time Series Approach for Leaf and Wood Classification from Terrestrial LiDAR Point
783 Clouds. *Remote Sensing* 14. doi:<https://doi.org/10.3390/rs14133157>.
- 784 Hildebrand, J., Schulz, S., Richter, R., Döllner, J., 2022. Simulating Lidar to Create Training Data for Machine Learning on 3D Point Clouds.
785 *ISPRS Annals of the Photogrammetry, Remote Sensing and Spatial Information Sciences X-4/W2-2022*, 105–112. doi:[https://doi.org/](https://doi.org/10.5194/isprs-annals-X-4-W2-2022-105-2022)
786 [10.5194/isprs-annals-X-4-W2-2022-105-2022](https://doi.org/10.5194/isprs-annals-X-4-W2-2022-105-2022).
- 787 Hopkinson, C., 2020. Data for: See the forest and the trees: Effective machine and deep learning algorithms for wood filtering and tree species
788 classification from terrestrial laser scanning. *Mendley Data V1*. doi:<https://doi.org/10.17632/4gbzk9sy24.1>.
- 789 Hurl, B., Czarnecki, K., Waslander, S., 2019. Precise Synthetic Image and LiDAR (PreSIL) Dataset for Autonomous Vehicle Perception, in: 2019
790 IEEE Intelligent Vehicles Symposium (IV), IEEE Press, p. 2522–2529. doi:<https://doi.org/10.1109/IVS.2019.8813809>.
- 791 Höfle, B., Pfeifer, N., 2007. Correction of laser scanning intensity data: Data and model-driven approaches. *ISPRS Journal of Photogrammetry*

792 and Remote Sensing 62, 415–433. doi:<https://doi.org/10.1016/j.isprsjprs.2007.05.008>.

793 Jaccard, P., 1901. Étude comparative de la distribution florale dans une portion des Alpes et des Jura. Bulletin del la Société Vaudoise des Sciences
794 Naturelles 37, 547–579.

795 Jutzi, B., Gross, H., 2009. NORMALIZATION OF LIDAR INTENSITY DATA BASED ON RANGE AND SURFACE INCIDENCE ANGLE. ISPRS - International Archives of the Photogrammetry, Remote Sensing and Spatial Information Sciences 38.
796

797 Krisanski, S., Taskhiri, M.S., Gonzalez Aracil, S., Herries, D., Muneri, A., Gurung, M.B., Montgomery, J., Turner, P., 2021a. Forest Structural
798 Complexity Tool—An Open Source, Fully-Automated Tool for Measuring Forest Point Clouds. Remote Sensing 13. doi:<https://doi.org/10.3390/rs13224677>.

799

800 Krisanski, S., Taskhiri, M.S., Gonzalez Aracil, S., Herries, D., Turner, P., 2021b. Sensor Agnostic Semantic Segmentation of Structurally Diverse
801 and Complex Forest Point Clouds Using Deep Learning. Remote Sensing 13, 1413. doi:<https://doi.org/10.3390/rs13081413>.

802 Krishna Moorthy, S.M., Calders, K., Vicari, M.B., Verbeeck, H., 2020. Improved Supervised Learning-Based Approach for Leaf and Wood
803 Classification From LiDAR Point Clouds of Forests. IEEE Transactions on Geoscience and Remote Sensing 58, 3057–3070. doi:<https://doi.org/10.1109/TGRS.2019.2947198>.

804

805 Kölle, M., Laupheimer, D., Schmohl, S., Haala, N., Rottensteiner, F., Wegner, J.D., Ledoux, H., 2021. The Hessigheim 3D (H3D) benchmark on
806 semantic segmentation of high-resolution 3D point clouds and textured meshes from UAV LiDAR and Multi-View-Stereo. ISPRS Open Journal
807 of Photogrammetry and Remote Sensing 1, 11. doi:<https://doi.org/10.1016/j.ophoto.2021.100001>.

808 Liu, C., Calders, K., Meunier, F., Gastellu-Etchegorry, J.P., Nightingale, J., Disney, M., Origo, N., Woodgate, W., Verbeeck, H., 2022. Implications
809 of 3D Forest Stand Reconstruction Methods for Radiative Transfer Modeling: A Case Study in the Temperate Deciduous Forest. Journal of
810 Geophysical Research: Atmospheres 127, e2021JD036175. doi:<https://doi.org/10.1029/2021JD036175>.

811 Matthews, B., 1975. Comparison of the predicted and observed secondary structure of T4 phage lysozyme. Biochimica et Biophysica Acta (BBA)
812 - Protein Structure 405, 442–451. doi:[https://doi.org/10.1016/0005-2795\(75\)90109-9](https://doi.org/10.1016/0005-2795(75)90109-9).

813 Momo Takoudjou, S., Ploton, P., Sonké, B., Hackenberg, J., Griffon, S., de Coligny, F., Kamdem, N.G., Libalah, M., Mofack, G.I., Le Mogueédec,
814 G., Péliissier, R., Barbier, N., 2018. Data from: Using terrestrial laser scanning data to estimate large tropical trees biomass and calibrate
815 allometric models: a comparison with traditional destructive approach. doi:<https://doi.org/10.5061/dryad.10hq7>.

816 Otepka, J., Ghuffar, S., Waldhauser, C., Hochreiter, R., Pfeifer, N., 2013. Georeferenced Point Clouds: A Survey of Features and Point Cloud
817 Management. ISPRS International Journal of Geo-Information 2, 1038–1065. doi:<https://doi.org/10.3390/ijgi2041038>.

818 Qi, C.R., Su, H., Mo, K., Guibas, L.J., 2017a. PointNet: Deep Learning on Point Sets for 3D Classification and Segmentation, in: 2017 IEEE
819 Conference on Computer Vision and Pattern Recognition (CVPR), pp. 77–85. doi:<https://doi.org/10.1109/CVPR.2017.16>.

820 Qi, C.R., Yi, L., Su, H., Guibas, L.J., 2017b. PointNet++: Deep Hierarchical Feature Learning on Point Sets in a Metric Space. arXiv preprint
821 arXiv:1706.02413 .

822 RIEGL Laser Measurement Systems, 2017. RIEGL VZ-400, Data Sheet. URL: [http://www.riegl.com/uploads/tx_pxpriegldownloads/](http://www.riegl.com/uploads/tx_pxpriegldownloads/10_DataSheet_VZ-400_2017-06-14.pdf)
823 [10_DataSheet_VZ-400_2017-06-14.pdf](http://www.riegl.com/uploads/tx_pxpriegldownloads/10_DataSheet_VZ-400_2017-06-14.pdf). last access: 2023-02-13.

824 RIEGL Laser Measurement Systems, 2022. RIEGL VUX-1LR, Data Sheet. [http://www.riegl.com/uploads/tx_pxpriegldownloads/](http://www.riegl.com/uploads/tx_pxpriegldownloads/RIEGL_VUX-1LR-22_Datasheet_2022-09-14.pdf)
825 [RIEGL_VUX-1LR-22_Datasheet_2022-09-14.pdf](http://www.riegl.com/uploads/tx_pxpriegldownloads/RIEGL_VUX-1LR-22_Datasheet_2022-09-14.pdf). Accessed: 2023-02-22.

826 Rousseau, D., Turgut, K., Dutagaci, H., 2022. Robustness of 3D point-based deep learning for plant organ segmentation against point density
827 variation and noise. doi:<https://doi.org/10.22541/au.166497086.66500223/v1>.

828 Schmohl, S., Sörgel, U., 2019. SUBMANIFOLD SPARSE CONVOLUTIONAL NETWORKS FOR SEMANTIC SEGMENTATION OF LARGE-
829 SCALE ALS POINT CLOUDS. ISPRS Annals of the Photogrammetry, Remote Sensing and Spatial Information Sciences IV-2/W5, 77–84.
830 URL: <https://isprs-annals.copernicus.org/articles/IV-2-W5/77/2019/>, doi:10.5194/isprs-annals-IV-2-W5-77-2019.

831 Shan, J., Toth, C., 2018. Topographic Laser Ranging and Scanning: Principles and Processing, Second Edition. CRC Press. doi:<https://doi.org/10.1201/9781315154381>.

832

833 Singer, N.M., Asari, V.K., 2021. DALES Objects: A Large Scale Benchmark Dataset for Instance Segmentation in Aerial Lidar. IEEE Access ,
834 1–1doi:10.1109/ACCESS.2021.3094127.

- 835 Sokolova, M., Lapalme, G., 2009. A systematic analysis of performance measures for classification tasks. *Information Processing & Management*
836 45, 427–437. doi:<https://doi.org/10.1016/j.ipm.2009.03.002>.
- 837 Solow, D., 2014. *Linear Programming: An Introduction to Finite Improvement Algorithms: Second Edition*. Dover Books on Mathematics, Dover
838 Publications.
- 839 Stewart, J., 2012. *Calculus : early transcendentals*. Brooks/Cole, Cengage Learning, Belmont, Cal.
- 840 Thomas, H., Qi, C.R., Deschaud, J.E., Marcotegui, B., Goulette, F., Guibas, L.J., 2019. KPConv: Flexible and Deformable Convolution for Point
841 Clouds. *Proceedings of the IEEE International Conference on Computer Vision*.
- 842 Triess, L.T., Rist, C.B., Peter, D., Zöllner, J.M., 2022. A Realism Metric for Generated LiDAR Point Clouds. *Int. J. Comput. Vision* 130,
843 2962–2979. doi:<https://doi.org/10.1007/s11263-022-01676-8>.
- 844 Vicari, M.B., Disney, M., Wilkes, P., Burt, A., Calders, K., Woodgate, W., 2019. Leaf and wood classification framework for terrestrial LiDAR
845 point clouds. *Methods in Ecology and Evolution* 10, 680–694. doi:<https://doi.org/10.1111/2041-210X.13144>.
- 846 Wang, C., Li, Q., Liu, Y., Wu, G., Liu, P., Ding, X., 2015. A comparison of waveform processing algorithms for single-wavelength LiDAR
847 bathymetry. *ISPRS Journal of Photogrammetry and Remote Sensing* 101, 22–35. doi:[https://doi.org/10.1016/j.isprsjprs.2014.](https://doi.org/10.1016/j.isprsjprs.2014.11.005)
848 11.005.
- 849 Wang, D., Momo Takoudjou, S., Casella, E., 2020. LeWoS: A universal leaf-wood classification method to facilitate the 3D modelling of large
850 tropical trees using terrestrial LiDAR. *Methods in Ecology and Evolution* 11, 376–389. doi:<https://doi.org/10.1111/2041-210X.13342>.
- 851 Wang, D., Takoudjou, S.M., Casella, E., 2021. LeWoS: A universal leaf-wood classification method to facilitate the 3D modelling of large tropical
852 trees using terrestrial LiDAR. doi:<https://doi.org/10.5061/dryad.np5hqbz6>.
- 853 Wang, Y., Sun, Y., Liu, Z., Sarma, S.E., Bronstein, M.M., Solomon, J.M., 2019. Dynamic Graph CNN for Learning on Point Clouds. *ACM*
854 *Transactions on Graphics* 38, 1–12. doi:<https://doi.org/10.1145/3326362>.
- 855 Weber, J., Penn, J., 1995. Creation and rendering of realistic trees, in: Mair, S.G., Cook, R. (Eds.), *Proceedings of the 22nd annual conference*
856 *on Computer graphics and interactive techniques - SIGGRAPH '95*, ACM Press, New York, New York, USA. pp. 119–128. doi:<https://doi.org/10.1145/218380.218427>.
- 857
- 858 Weinmann, M., Urban, S., Hinz, S., Jutzi, B., Mallet, C., 2015. Distinctive 2D and 3D features for automated large-scale scene analysis in urban
859 areas. *Computers & Graphics* 49, 47–57. doi:<https://doi.org/10.1016/j.cag.2015.01.006>.
- 860 Weiser, H., Schäfer, J., Winiwarter, L., Krašovec, N., Fassnacht, F.E., Höfle, B., 2022. Individual tree point clouds and tree measurements
861 from multi-platform laser scanning in German forests. *Earth System Science Data* 14, 2989–3012. doi:[https://doi.org/10.5194/](https://doi.org/10.5194/essd-14-2989-2022)
862 [essd-14-2989-2022](https://doi.org/10.5194/essd-14-2989-2022).
- 863 Weiser, H., Schäfer, J., Winiwarter, L., Krašovec, N., Seitz, C., Schimka, M., Anders, K., Baete, D., Braz, A.S., Brand, J., Debroize, D., Kuss, P.,
864 Martin, L.L., Mayer, A., Schrempp, T., Schwarz, L.M., Ulrich, V., Fassnacht, F.E., Höfle, B., 2021. Terrestrial, UAV-borne, and airborne laser
865 scanning point clouds of central European forest plots, Germany, with extracted individual trees and manual forest inventory measurements.
866 doi:<https://doi.org/10.1594/PANGAEA.933426>.
- 867 Weiser, H., Ulrich, V., Winiwarter, L., Esmoris, A.M., Höfle, B., 2023. Manually labeled terrestrial laser scanning point clouds of individual trees
868 for leaf-wood separation. doi:<https://doi.org/10.11588/data/UUMEDI>.
- 869 Weiser, H., Winiwarter, L., Anders, K., Fassnacht, F.E., Höfle, B., 2021. Opaque voxel-based tree models for virtual laser scanning in forestry
870 applications. *Remote Sensing of Environment* 265, 112641. doi:<https://doi.org/10.1016/j.rse.2021.112641>.
- 871 Winiwarter, L., Esmoris Pena, A.M., Weiser, H., Anders, K., Martínez Sánchez, J., Searle, M., Höfle, B., 2022. Virtual laser scanning with
872 HELIOS++: A novel take on ray tracing-based simulation of topographic full-waveform 3D laser scanning. *Remote Sensing of Environment*
873 269. doi:<https://doi.org/10.1016/j.rse.2021.112772>.
- 874 Winiwarter, L., Mandlbürger, G., Schmohl, S., Pfeifer, N., 2019. Classification of ALS Point Clouds Using End-to-End Deep Learning. *PFG – Jour-*
875 *nal of Photogrammetry, Remote Sensing and Geoinformation Science* 87, 75–90. doi:<https://doi.org/10.1007/s41064-019-00073-0>.
- 876 Wu, B., Wan, A., Yue, X., Keutzer, K., 2018. SqueezeSeg: Convolutional Neural Nets with Recurrent CRF for Real-Time Road-Object Segmen-
877 tation from 3D LiDAR Point Cloud, in: *2018 IEEE International Conference on Robotics and Automation (ICRA)*, IEEE Press. p. 1887–1893.

878 doi:<https://doi.org/10.1109/ICRA.2018.8462926>.

879 Wu, B., Zheng, G., Chen, Y., 2020. An Improved Convolution Neural Network-Based Model for Classifying Foliage and Woody Components from
880 Terrestrial Laser Scanning Data. *Remote Sensing* 12, 1010. doi:<https://doi.org/10.3390/rs12061010>.

881 Xi, Z., Hopkinson, C., Rood, S.B., Peddle, D.R., 2020. See the forest and the trees: Effective machine and deep learning algorithms for wood
882 filtering and tree species classification from terrestrial laser scanning. *ISPRS Journal of Photogrammetry and Remote Sensing* 168, 1–16.
883 doi:<https://doi.org/10.1016/j.isprsjprs.2020.08.001>.

884 Zahs, V., Anders, K., Kohns, J., Stark, A., Höfle, B., 2023. Classification of structural building damage grades from multi-temporal pho-
885 togrammetric point clouds using a machine learning model trained on virtual laser scanning data. *International Journal of Applied Earth*
886 *Observation and Geoinformation* 122, 103406. URL: <https://www.sciencedirect.com/science/article/pii/S1569843223002303>,
887 doi:<https://doi.org/10.1016/j.jag.2023.103406>.

888 Zhang, X.D., 2017. *Matrix Analysis and Applications*. Cambridge University Press. doi:<https://doi.org/10.1017/9781108277587>.